scientific reports

Check for updates

OPEN

Multilayered quantum computing and simulation system for enhanced image representation of HSI based Fourier transform and adjacency matrix

Nawres A. Alwan[1], Suzan J. Obaiys[1]✉, Nadia M. G. Al-Saidi[2], Nurul Fazmidar Binti Mohd Noor[1] & Yeliz Karaca[3,4]

Quantum image processing, as a convergence of quantum computing and image processing, necessitates extensive research into quantum image representations (QIRs), which are among the most significant topics shaping the field of quantum computing (QC) due to their potential opportunities and challenges. This study introduces a novel QIR model based on the hue, saturation, and intensity (HSI) colour model. Our model advances image encoding by uniquely integrating an adjacency matrix to capture spatial pixel relationships with a Fourier transform (FT) representation for pixel intensity. Based on the HSI color space, AFQIRHSI uses a dual-entanglement structure; one state links the adjacency and intensity information, while another efficiently encodes hue and saturation. Named the adjacency Fourier quantum image representation of HSI (AFQIRHSI), this model utilises $2n + p + 3$ qubits to store a colour digital image of size $2^n \times 2^n$. AFQIRHSI enhances storage capacity by factors of four and two compared to earlier models, such as QIRHSI and EQIRHSI. In this paper, we also present several quantum image operations, including complement colour transformation (U_{CC}), global colour transformation (U_{st}), quantum image retrieval (S_{ct}), and quantum image detection (QED). Comparative analyses of various quantum image representations are provided, highlighting their similarities and differences. AFQIRHSI offers a robust foundation for advanced quantum image processing applications, particularly in medical imaging and AI-based image classification.

Quantum image processing, an emerging technology, explores the integration of quantum computing and quantum information, enabling cross-disciplinary advancements that address quantum information processing across various fields while considering the theoretical and physical aspects of quantum image processing. Building on foundational knowledge of quantum information and computing, this concept has been introduced to address inefficiencies inherent in tasks performed by classical computation[1]. Quantum computing has demonstrated advantages over classical computing in terms of data storage and computational efficiency, owing to its unique characteristics, including quantum coherence, superposition of quantum states, and fragmentation[2]. Consequently, research efforts are focused on enhancing the effectiveness of image processing and computational performance by leveraging quantum computing. Quantum image processing has emerged as a critical area in the era of quantum computers, encompassing quantum image representations (QIR), quantum image processing algorithms, and quantum image measurement. This field requires rigorous preparation of quantum images, detailed analysis of the quantum bits involved, and assessment of their computational complexity[3].

Quantum image processing (QIP), grounded in quantum mechanics, enables advanced image storage and processing by using orthogonal image representations and qubit-based systems. Recent progress in QIP has led to breakthroughs in QIR, with applications extending to AI and machine learning on quantum platforms.

[1]Department of Computer System & Technology, Faculty of Computer Science and Information Technology, Universiti Malaya, Kuala Lumpur 50603, Malaysia. [2]Department of Applied Sciences, University of Technology, Baghdad 10066, Iraq. [3]University of Massachusetts Chan Medical School (UMASS), 55 Lake Avenue North, MA 01655 Worcester, USA. [4]Massachusetts Institute of Technology (MIT), 77 Massachusetts Avenue, MA 02139 Cambridge, USA. ✉email: suzan@um.edu.my

These developments push the boundaries of quantum information processing beyond classical quantum computing which is used the bits. Since its inception in 1982, the field of quantum computation has progressed through critical theoretical developments and promising experimental results[4]. Notably, Shor introduced the quantum integer factoring algorithm in 1995, which operates in polynomial time[5], and Grover presented a novel quantum search algorithm for databases in 1997, offering quadratic acceleration[6]. These algorithms have been instrumental in advancing quantum computing. Quantum computation benefits from the unique properties of quantum mechanics, such as superposition and entanglement, to store, process, and transmit information[7]. Its applications span various fields, including information theory, cryptography, and image processing[8]. Digital image processing (DIP), a significant branch of computer science, is integral to many applications[9]. The rapid advancement of image and video capture technologies, particularly on mobile devices and computers, has resulted in an exponential increase in visual content. Consequently, there is a pressing need to develop and deploy algorithms capable of efficiently managing visual data, including local and remote tasks such as face recognition[10,11]. Despite these advancements, the early development of quantum computers presented challenges, particularly in representing images in quantum states and preparing and processing quantum images on quantum computers. These remain key hurdles in the field.

QIP bridges quantum computing and image analysis, offering advantages like exponential storage gains and quantum features such as entanglement and parallelism[4,12–14]. It encompasses quantum image representation and processing algorithms to enhance visual data handling. Recent advancements include applications in quantum watermarking, steganography, and encryption[15–23].

In QIP, numerous algorithms have been developed for image retrieval, storage, compression, and processing using quantum mechanics. Examples include qubit lattice[24], entangled images[25], real ket[26], flexible representation of quantum images (FRQI)[8], multi-channel representation for quantum images (MCRQI)[27], normal arbitrary quantum superposition state (NAQSS)[28], bit plane representation of quantum images (BRQI)[29], novel enhanced quantum representation of digital images (NEQR)[30], multi-channel representation for quantum images (MCQI)[31], novel quantum representation of colour digital images (NCQI)[32], generalised quantum image representation (GQIR)[33], RGB multi-channel representation for quantum coloured images (QMCR)[34], quantum representation of multi-wavelength (QRMW)[35], quantum representation of colour images (QRCI)[36], and double quantum representation of colour images (DQRCI)[37]. Several scholars have also introduced quantum image representation models based on Fourier transformations[38]-[40]. In 2020, Artyom et al.[39] proposed a model for representing discrete signals and images in quantum form using the quantum Fourier transform (QFT). Over the last decade, many researchers have studied hue, saturation, and intensity (HIS) and hue, saturation, and lightness (HSL) colour spaces[41–43]. Yan et al.[44] introduced the quantum hue, saturation, and lightness (QHSL) colour model, which represents information using qubits and stores lightness data in a sequence of q qubits. In 2022, a novel quantum image representation, quantum image representation for HSI (QIRHSI), was proposed[45]. QIRHSI integrates FRQI and NEQR models. In 2023, an enhanced method called the Enhanced Quantum Image Representation for HSI Colour Model (EQIRHSI) was introduced[46]. EQIRHSI builds on QIRHSI but employs entangled states for hue (H) and saturation (S) instead of superposition From these developments, it is evident that most QIR models derive from three foundational methods: FRQI, NEQR, and NASS: (1) FRQI relies on the amplitude of quantum states (probabilistic); (2) NEQR directly encodes pixel intensity values using binary representation (deterministic); (3) NASS maps each pixel's intensity and location onto a superposition of quantum states. Some approaches apply NEQR to colour images, while others adapt FRQI or use hybrid methods, such as QIRHSI and EQIRHSI. Notably, EQIRHSI introduces an innovative use of entanglement between hue (H) and saturation (S) qubits, allowing the transformation of information based on entangled states. Furthermore, authors in[50] proposed a novel representation method using two hybrid-qubit entangled quantum registers comprising seven qutrits. Despite these advancements, none of the existing models define a formula to capture relationships between neighbouring pixels in an image. This omission represents a significant limitation, which we aim to address with the AFQIRHSI. This paper is the first to propose a solution for this gap by introducing a method that identifies pixel similarities using an adjacency matrix and entanglement states.

QIP has emerged as a promising solution to growing demands in data storage, transmission, and computational power. By leveraging quantum systems to encode and process image data, researchers aim to tackle challenges that classical methods struggle with. Despite progress, the potential of quantum techniques for accelerating signal processing remains largely untapped[13,51].

Motivated by the outlined background and challenges, the current work aims to propose a new QIR based on the HSI colour space. This model leverages two fundamental principles of quantum mechanics - superposition and entanglement states - simultaneously, resulting in a comprehensive QIR model. Named adjacency Fourier quantum image representation of HSI (AFQIRHSI), this method integrates features from the EQIRHSI and quantum Fourier transform (QFT) models, offering an enhanced representation of quantum images. Our proposed model for representing an image of size $2^n \times 2^n$ requires $2n + p + 3$ qubits: $2n$ qubits for storing the pixel position information, p qubits for adjacency information (adjacency matrix), and three qubits to encode the H, S, and I components, with one qubit assigned to each. In our model $p = 4$. The model's efficiency stems from its dual entanglement structure, which significantly enhances its capabilities compared to other methods. First, the entanglement between the H and S components enables smooth and efficient encoding of colour information. This ensures that the H and S values of each pixel are inherently linked, resulting in a more natural and accurate colour representation at the quantum mechanics level. Second, the entanglement between the adjacency matrix and the Fourier-transformed intensity values adds robustness and complexity to the model. These two entanglement mechanisms work in tandem to provide a comprehensive and efficient approach to image representation in the context of QIP. The AFQIRHSI model demonstrates superiority in handling complex image data with greater precision and efficiency than existing quantum image representation

Quantum Image Representation	Type	Required Qubits	Color Encoding	Color	Grey
FRQI	Probabilistic	$2n+1$	1 angle vector (greyscale)	-	✓
QIRHSI	Probabilistic/ Deterministic	$2n+q+2$	2 superimposed angle vectors and q qubits sequence (HSI)	✓	✓
EQIRHSI	Probabilistic/ Deterministic	$2n+q+2$	2 entangled angle vectors and q qubits sequence (HSI)	✓	✓
FTQR	Phase-Based Intensity	$r+s+1$	s+1 qubits sequence (RGB)	✓	✓
AFQIRHSI	Probabilistic/ Deterministic	$2n+p+3$	2 entangled angle vectors and 4 qubits sequence (HSI) + adjacency matrix	✓	✓

Table 1. Comparison of various QIR models: FRQI, QIRHSI, EQIRHSI and AFQIRHSI.

QIR Model	Complexity
FRQI	$O\left(2^{4n}\right)$
QIRHSI	$O\left(2^{4n+2}+qn\cdot 2^{2n}\right)$
EQIRHSI	$O\left(8\cdot 2^{4n}+qn\cdot 2^{2n}\right)$
AFQIRHSI	$O\left(4\cdot 2^{4n}+2n+4-2^{2n}\right)$

Table 2. Comparison of the Complexity of Various Models.

methods. Table 1 provides a comparison of several QIR models, including FRQI, QIRHSI, EQIRHSI, and the proposed AFQIRHSI. Based on our comparative analysis, the key characteristics of these models are as follows:

- QIRHSI employs a superposition state of two qubits to encode H and S information. In contrast, EQIRHSI utilises an entangled two-qubit state, enabling classical image restoration by measuring only the probability information of either the H or S channel. This approach significantly enhances image retrieval efficiency. AFQIRHSI further improves upon this by incorporating adjacency matrices, which are especially effective for edge detection and complex image manipulations. The use of adjacency matrices and the FT enables more detailed and accurate image representation. Specifically, AFQIRHSI encodes H and S using an entangled two-qubit state, while adjacency information and intensity (I) are encoded through a combination of two-qubit entanglement and the FT.
- EQIRHSI requires the probability amplitude of only two qubits to represent an image, compared to MCQI, which needs three qubits. This makes EQIRHSI more flexible for quantum image representation. AFQIRHSI builds on this flexibility by incorporating adjacency matrices, allowing it to handle intricate image structures and pixel relationships with greater ease and versatility.
- The QIRHSI model requires $2n+24$ qubits to represent a $2^n \times 2^n$ quantum colour image, while EQIRHSI reduces this to $2n+10$ qubits. Both models have comparable preparation complexity at $n\cdot 2^{4n}$. Despite adding adjacency matrices and the FT, AFQIRHSI maintains similar complexity while offering enhanced functionality (see Table 2).
- EQIRHSI requires only one operation to simultaneously modify H and S channel information, whereas QIRHSI requires two. AFQIRHSI retains this convenience while offering superior handling of image edges and details through its adjacency-based approach (see Section 6.5). This makes it more efficient and effective for comprehensive image transformations.
- For applications in quantum information processing (QIP), such as quantum edge detection and quantum cryptography, AFQIRHSI outperforms QIRHSI and EQIRHSI. Its use of entanglement between adjacency matrices and the FT enhances edge detection by accurately capturing relationships between neighbouring pixels. The FT also strengthens cryptographic security through complex, hard-to-decrypt transformations. Consequently, AFQIRHSI is particularly effective in QIP applications, including quantum image representation and secure image encryption.

The remainder of this paper is organised as follows. Section 2 reviews related work on QIR. Section 3 outlines fundamental concepts, including HSI, adjacency matrices, and basic quantum gates. Section 4 describes the preparation of AFQIRHSI model images. Section 5 discusses QIR operations, such as image retrieval and edge detection. Finally, Section 6 summarises the paper. Figure 1 illustrates the AFQIRHSI Model for Quantum Image Representations and Operations.

Related work

Several models have been proposed for storing and processing images using QIR technology. The qubit lattice model[24] introduces a novel approach, where each pixel is stored in a single qubit, and all pixel operations are converted into their quantum counterparts on individual qubits. Consequently, each quantum image is represented as a matrix of qubits. The entangled image model[25] utilises quantum entanglement to store and retrieve images. The real ket model[26] focuses on performing a quadtree operation on the image repeatedly to create a balanced quadtree index, with each pixel mapped onto a basic state within a quadratic sequence of qubits. The flexible representation of quantum images (FRQI) model[8] stores pixel position information in the base state of a two-dimensional qubit sequence, while colour information is represented as the probability amplitude of a single qubit in combination with the qubit sequence. The novel enhanced quantum representation (NEQR)[30] presents an improved quantum image representation. More details on quantum image representation models and operations can be found in references[3,16,32].

The FRQI model[8] uses two qubits to represent the position (x, y) of each pixel, while one qubit is used to represent the colour information. The colour information is then tensor-multiplied with the qubit sequence of a $2^n \times 2^n$ image. Figure 2 and Eq. 3 illustrate a 2×2 colour image and its corresponding FRQI representation. The mathematical description of the FRQI model can be defined as follows:

$$\begin{aligned} |I(\theta)\rangle &= \frac{1}{2^n} \sum_{k=0}^{2n-1} (\cos\theta_k|0\rangle + \sin\theta_k|1\rangle) \otimes |k\rangle, \\ \theta_k &\in \left[0, \frac{\pi}{2}\right], k = 0, 1, \ldots, 2^{2n} - 1 \end{aligned} \tag{1}$$

The NEQR model [30] uses two qubits to represent the (x, y) position of each pixel, while 8 qubits are used to represent the grey colour information. These are then tensor-multiplied with the qubit sequence for a $2^n \times 2^n$ image. Figure 3 and Eq. 4 illustrate a 2×2 grey image along with its corresponding NEQR representation. The mathematical description of the NEQR model is defined as follows:

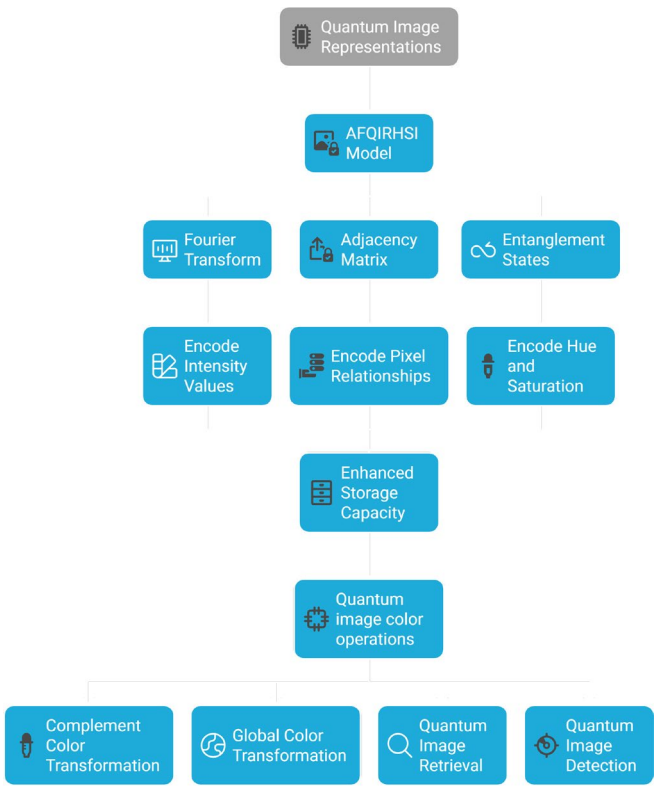

Fig. 1. AFQIRHSI Model for Quantum Image Representations and Operations.

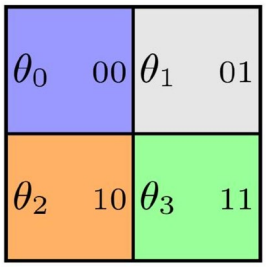

Fig. 2. Simple image with its FRQI state[8].

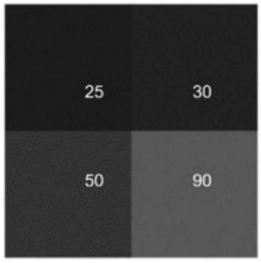

Fig. 3. Simple image with its NERQ state.

$$|I\rangle = \frac{1}{2^n}\sum_{y=0}^{2^n-1}\sum_{x=0}^{2^n-1}\sum_{k=0}^{q-1}\left|C_{yx}^{k}\right\rangle|yx\rangle \tag{2}$$

where $C_{yx}^{i} = C_{yx}^{0}C_{yx}^{1}\ldots C_{yx}^{q-2}C_{yx}^{q-1}$ and $C_{yx}^{i} \in \{0,1\}$.

$$\begin{aligned}|I\rangle = \frac{1}{2}\big[&(\cos\theta_0|0\rangle + \sin\theta_0|1\rangle)\otimes|00\rangle\\ &+(\cos\theta_1|0\rangle + \sin\theta_1|1\rangle)\otimes|01\rangle\\ &+(\cos\theta_2|0\rangle + \sin\theta_2|1\rangle)\otimes|10\rangle\\ &+(\cos\theta_3|0\rangle + \sin\theta_3|1\rangle)\otimes|11\rangle\big].\end{aligned} \tag{3}$$

$$\begin{aligned}|I\rangle = \frac{1}{2}\big[&|00011001\rangle|00\rangle + |00011110\rangle|01\rangle +\\ &|00110010\rangle|10\rangle + |01011010\rangle|11\rangle\big].\end{aligned} \tag{4}$$

In 2020, Artyom et al.[39] introduced a new method for representing images and discrete digital signals, called Fourier transform qubit representation (FTQR). The FTQR model fundamentally relies on the representation of qubits through the Fourier transform. For greyscale images, this model adopts a comparable approach to the Fourier representation of images. For colour images, it introduces methodologies that utilise the concept of a 3-point discrete Fourier transform (DFT) for colour qubits. The representation of the signal of r-qubits is defined as:

$$|\mathscr{R}\rangle = \frac{1}{\sqrt{N}}\sum_{k=0}^{N-1} e^{i\alpha\Re_\ell}|\ell\rangle \tag{5}$$

where $\theta = 2\pi/1024$. The term $e^{i\alpha\Re_\ell}|\ell\rangle$ maps classical intensity values (0, 255) into the imaginary plane $(x + i\cdot y)$. Here, $\Re_\ell$ represents the input signal at coordinate ℓ, which expands to x and y.

The representation of a greyscale or colour image with size $i \times j$ is defined as

$$|\breve{\Re}\rangle = \frac{1}{\sqrt{MN}}\sum_{m=0}^{M-1}\sum_{n=0}^{N-1} e^{i\alpha\Re_{n,m}|i,j\rangle} \tag{6}$$

This model requires $(\mathrm{n} + m + 1)$ qubits.

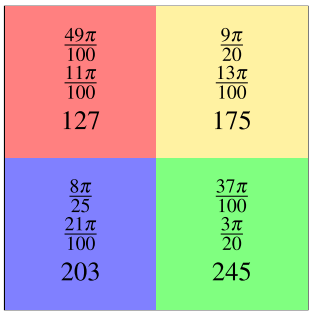

Fig. 4. QIRHSI for a 2×2 image, along with its corresponding quantum circuit and state configuration.

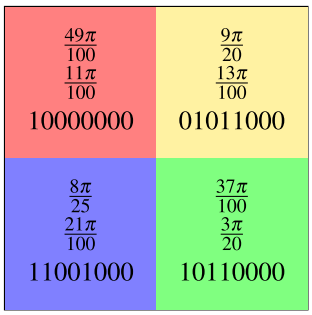

Fig. 5. EQIRHSI for a 2×2 image.

Based on the HIS colour model, several authors have introduced quantum image representation models, such as the quantum image representation HSI colour model (QIRHSI)[45] and the enhanced quantum image representation HSI colour model (EQIRHSI)[46]. In the QIRHSI model, the hue (H) and saturation (S) are represented using two qubits, while intensity (I) is depicted through multiple binary qubits.

The mathematical representation of QIRHSI is given as follows:

$$|I(\theta)\rangle = \frac{1}{2^n}\sum_{k=0}^{2^{2e}-1}|C_k\rangle \otimes |k\rangle = \frac{1}{2^n}\sum_{k=0}^{2^{2n}-1}|H_k\rangle\,|S_k\rangle\,|I_k\rangle \otimes |k\rangle \tag{7}$$

This format is a summation over k, ranging from 0 to $2^{2n}-1$, combining the colour information $|C_k\rangle$ with the pixel position $|k\rangle$, where each is normalised by $\frac{1}{2^n}$. The colour information is further broken down into hue ($|H_k\rangle$), saturation ($|S_k\rangle$), and intensity ($|I_k\rangle$) components. These components are described as follows: $|H_k\rangle$ and $|S_k\rangle$ are defined using trigonometric functions of angles θ_{hk} and θ_{sk}, respectively, with these angles ranging from 0 and $\frac{\pi}{2}$. The intensity component $|I_k\rangle$ is represented by a string of qubits, $\left|C_k^0 C_k^1 \ldots C_k^{q-2} C_k^{q-1}\right\rangle$, where each C_k^m is either 0 or 1.

Specifically,

$$\begin{gathered}
|H_k\rangle = \cos\theta_{hk}|0\rangle + \sin\theta_{hk}|1\rangle \\
|S_k\rangle = \cos\theta_{sk}|0\rangle + \sin\theta_{sk}|1\rangle \\
|I_k\rangle = \left|C_k^0 C_k^1 \ldots C_k^{q-2} C_k^{q-1}\right\rangle \\
\theta_{hk}, \theta_{sk} \in [0, \pi/2], C_k^m \in \{0, 1\} \\
m = 0, 1, \ldots, q-1 \\
k = 0, 1, \ldots, 2^{2n}-1
\end{gathered}$$

The pixel position $|k\rangle$ is encoded in a $2n$-qubit system, where the vertical and horizontal coordinates are represented as $|y\rangle$ and $|x\rangle$, respectively. These are further broken down into binary representations $|y_{n-1}\ldots y_1 y_0\rangle$ and $|x_{n-1}\ldots x_1 x_0\rangle$. Figure 4 and Eq. 9 illustrate a 2×2 QIRHSI image, along with its corresponding quantum circuit and state representation. The number of qubits required to represent the quantum image using the QIRHSI model is $\left(2\left(2^{m+n}\right) + q2^{m+n} + m + n\right)$ qubits.

While the EQIRHSI model is similar to QIRHSI, it incorporates an entanglement state for representing the hue (H) and saturation (S) components. Figure 5 and Eq. 10 illustrate a 2×2 QIRHSI image, along with its

corresponding quantum circuit and state representation. The mathematical representation of EQIRHSI is given as follows:

$$|I(\theta)\rangle = \frac{1}{2^{n+\frac{1}{2}}} \sum_{k=0}^{2^{2n}-1} \left(\cos\theta_k^n|00\rangle + \cos\theta_k^s|01\rangle + \sin\theta_k^h|10\rangle + \sin\theta_k^s|11\rangle\right) \otimes \left|C_k^0 C_k^1 \cdots C_k^{q-1}\right\rangle \otimes |k\rangle \quad (8)$$

Where

$$\begin{cases} |H_k S_k\rangle = \cos\theta_k^h|00\rangle + \cos\theta_k^s|01\rangle + \sin\theta_k^h|10\rangle + \sin\theta_k^s|11\rangle \\ |I_k\rangle = \left|C_k^0 C_k^1 \cdots C_k^{q-1}\right\rangle \\ \left\{\theta_k^h, \theta_k^s\right\} \in \left[0, \frac{\pi}{2}\right] \\ C_k^m \in \{0,1\} \\ m = 0, 1, \cdots, q-1 \\ k = 0, 1, \ldots, 2^{2n-1} \end{cases}$$

$$\begin{array}{ll} & |H_{yx}\rangle \\ & |S_{yx}\rangle \\ \text{Color:} & \left|C_{yx}^0\right\rangle \\ & \vdots \\ & \left|C_{yx}^6\right\rangle \\ & \left|C_{yx}^7\right\rangle \\ Y \text{ Axis:} & |y_0\rangle \\ X \text{ Axis:} & |x_0\rangle \end{array} \quad (9)$$

$$\begin{aligned} |I(\theta)\rangle = \frac{1}{2} \quad & \left[\left(\cos\frac{49\pi}{100}|0\rangle + \sin\frac{49\pi}{100}|1\rangle\right)\left(\cos\frac{11\pi}{100}|0\rangle + \sin\frac{11\pi}{100}|1\rangle\right)|01111111\rangle \otimes |00\rangle\right. \\ & + \left(\cos\frac{9\pi}{20}|0\rangle + \sin\frac{9\pi}{20}|1\rangle\right)\left(\cos\frac{13\pi}{100}|0\rangle + \sin\frac{13\pi}{100}|1\rangle\right)|10101111\rangle \otimes |01\rangle \\ & + \left(\cos\frac{8\pi}{25}|0\rangle + \sin\frac{8\pi}{25}|1\rangle\right)\left(\cos\frac{21\pi}{100}|0\rangle + \sin\frac{21\pi}{100}|1\rangle\right)|11001011\rangle \otimes |10\rangle \\ & \left. + \left(\cos\frac{37\pi}{100}|0\rangle + \sin\frac{37\pi}{100}|1\rangle\right)\left(\cos\frac{3\pi}{20}|0\rangle + \sin\frac{3\pi}{20}|1\rangle\right)|11110101\rangle \otimes |11\rangle\right] \end{aligned}$$

$$\begin{array}{ll} & |H_{yx}\rangle \\ & |S_{yx}\rangle \\ \text{Color:} & \left|C_{yx}^0\right\rangle \\ & \vdots \\ & \left|C_{yx}^6\right\rangle \\ & \left|C_{yx}^7\right\rangle \\ Y \text{ Axis:} & |y_0\rangle \\ X \text{ Axis:} & |x_0\rangle \end{array} \quad (10)$$

$$\begin{aligned} |I\rangle = \frac{1}{2^{\frac{3}{2}}} \Bigg[& \left(\cos\theta_0^k|00\rangle + \cos\theta_0^s|01\rangle + \sin\theta_0^l|10\rangle + \sin\theta_0^s|11\rangle\right)|10000000\rangle \otimes |00\rangle \\ & + \left(\cos\theta_1^l|00\rangle + \cos\theta_1^s|01\rangle + \sin\theta_1^h|10\rangle + \sin\theta_1^s|11\rangle\right)|01011000\rangle \otimes |01\rangle \\ & + \left(\cos\theta_2^b|00\rangle + \cos\theta_2^v|01\rangle + \sin\theta_2^k|10\rangle + \sin\theta_2^s|11\rangle\right)|11001000\rangle \otimes |10\rangle \\ & + \left(\cos\theta_3^b|00\rangle + \cos\theta_3^s|01\rangle + \sin\theta_3^k|10\rangle + \sin\theta_3^s|11\rangle\right)|10110000\rangle \otimes |11\rangle \Bigg]. \end{aligned}$$

Fundamental concepts

In this section, we introduce some basic concepts of quantum operations, quantum gates, circuits and database. The Hadamard gate (H) also known as the Hadamard operator, is a fundamental quantum gate used in quantum computing. It is represented by a unitary matrix and is used to manipulate qubits in a quantum circuit. The Hadamard gate maps the basis state to an equal superposition of the two basis states, creating a state of quantum superposition. It can be thought of as a 90° rotation around the Y -axis, followed by a 180° rotation around the X -axis. The Hadamard gate is defined as:

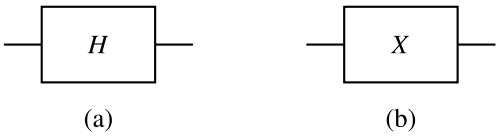

Fig. 6. (**a**) Hadamard gate and (**b**) *X* (NOT) gate circuit.

Name	Representing Matrix	Circuit
a) Controlled- NOT Gate	$\mathrm{CNOT} = \begin{bmatrix} 1 & 0 & 0 & 0 \\ 0 & 1 & 0 & 0 \\ 0 & 0 & 0 & 1 \\ 0 & 0 & 1 & 0 \end{bmatrix}$	$\lvert a\rangle$ — $\lvert a\rangle$; $\lvert b\rangle$ — $\lvert a \oplus b\rangle$ C-NOT gate
b) SWAP Gate	$\mathrm{SWAP} = \begin{bmatrix} 1 & 0 & 0 & 0 \\ 0 & 0 & 1 & 0 \\ 0 & 1 & 0 & 0 \\ 0 & 0 & 0 & 1 \end{bmatrix}$	$\lvert a\rangle$ — $\lvert b\rangle$; $\lvert b\rangle$ — $\lvert a\rangle$ SWAP gate

Table 3. Examples of Two-Qubit Gates: (a) Controlled NOT (CNOT) Gate and (b) SWAP Gate.

$$H = \frac{1}{\sqrt{2}} \begin{pmatrix} 1 & 1 \\ 1 & -1 \end{pmatrix} \tag{11}$$

Figure 6 (a) shows the Hadamard gate circuit. The *X* gate, also known as the NOT gate or Pauli- *X* gate, is a single-qubit quantum gate used in quantum circuit simulation. It is the quantum equivalent of the classical NOT gate. Figure 6 (b) shows the NOT gate circuit:

The *H* gate is both Hermitian and unitary, and it transforms operators acting in a 2*D* Hilbert space.

Some examples of two- and three-qubit gates include the CNOT gate and the SWAP gate, as shown in Table 3. The operations of the CNOT gate and SWAP gate are defined as follows.

HSI colour space in image processing

In image processing, hue (H) reflects the spectral wavelength closest to the colour, distinguishing between different colour categories such as red, blue, or green. Saturation (S) measures the intensity or purity of the colour; higher saturation indicates a more vivid and vibrant colour, while lower saturation results in a more washed-out or greyish colour. Intensity (I) corresponds to the amount of light reflected by the object, influenced by the object's reflection coefficient and the light's intensity. The RGB colour model does not align well with human colour perception. In contrast, the HSI model provides a more intuitive description of colour properties.

To normalise the RGB colour values, we use: $R' = \frac{R}{255}, G' = \frac{G}{255}$, and $B' = \frac{B}{255}$. Then, to calculate the *I*, the formula is:

$$I = \frac{R' + G' + B'}{3} \tag{12}$$

For the *S*, we use:

$$S = 1 - \frac{3m}{R' + G' + B'} \tag{13}$$

where $\min(R', G', B') = m$

If $R' = G' = B'$, then $S = 0$.

To calculate *H*, we use:

$$H = \cos^{-1}\left(\frac{0.5\left[(R' - G') + (R' - B')\right]}{\sqrt{(R' - G')^2 + (R' - B')(G' - B')}}\right) \tag{14}$$

if $B' > G'$, then $H = 360^\circ - H$.

When converting from HSI to RGB, the applicable equations depend on the value of *H* If $0^\circ \leq H < 120^\circ$ or $[0, 2\pi/3]$:

$$B = I(1 - S) \tag{15}$$

$$R = I\left[1 + \frac{S\cos H}{\cos(60^\circ - H)}\right] \tag{16}$$

$$G = 3I - (R + B) \tag{17}$$

If $120^\circ \leq H < 240^\circ [2\pi/3, 4\pi/3]$:

$$H = H - 120^\circ \tag{18}$$

$$R = I(1 - S) \tag{19}$$

$$G = I\left[1 + \frac{S\cos H}{\cos(60^\circ - H)}\right] \tag{20}$$

$$B = 3I - (R + G) \tag{21}$$

If $240^\circ \leq H \leq 360^\circ$ or $\left[\frac{4\pi}{3}, 2\pi\right]$:

$$G = I(1 - S) \tag{22}$$

$$B = I\left[1 + \frac{S\cos H}{\cos(60^\circ - H)}\right] \tag{23}$$

$$R = 3I - (G + B) \tag{24}$$

The HSI colour model can be depicted geometrically as shown in Figure 7.

Figure 8 (a, c) shows the RGB image, while (b, d) displays the corresponding HSI image. Figure 9 presents (a) Carole Hersee, along with the corresponding (b) H, (c) S, and (d) I components.

Adjacency matrix for colour

The relationship between adjacent colours can be encoded using the entanglement state through the adjacency matrix. The adjacency matrix, A_{ij}, is defined as $A_{ij} = 1$ if colours i and j are adjacent and $A_{ij} = 0$ otherwise. For example, if we have three colours, the adjacency matrix A is defined as follows:

$$A = \begin{pmatrix} 0 & 1 & 0 & 0 \\ 1 & 0 & 0 & 0 \\ 0 & 0 & 0 & 0 \\ 0 & 0 & 0 & 0 \end{pmatrix} \tag{25}$$

To represent the adjacency matrix, we use a controlled-NOT (CNOT) gate (see Table 3 a). The adjacency vectors for each pixel in the image are calculated based on the similarity relationship, which is defined as[49]:

$$\text{similarity} = \frac{\text{A} \cdot \text{B}}{|\text{A}| \cdot | \cdot |\text{B}||} \tag{26}$$

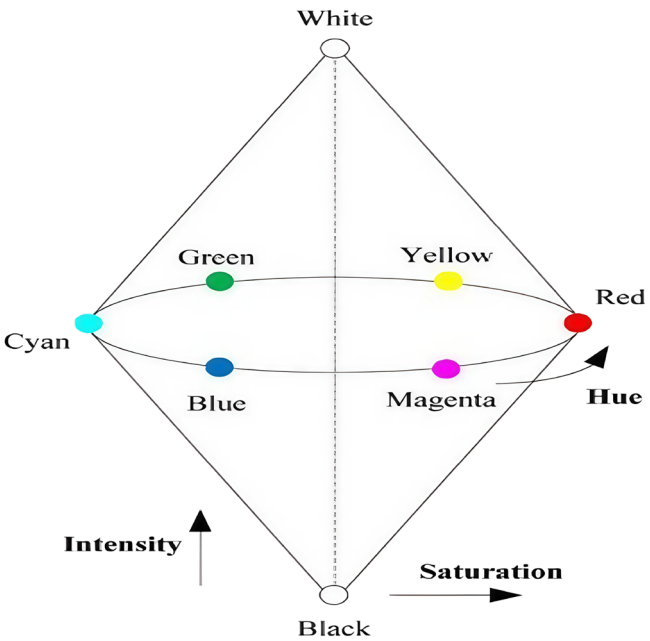

Fig. 7. Geometric depiction of the HSI colour model.

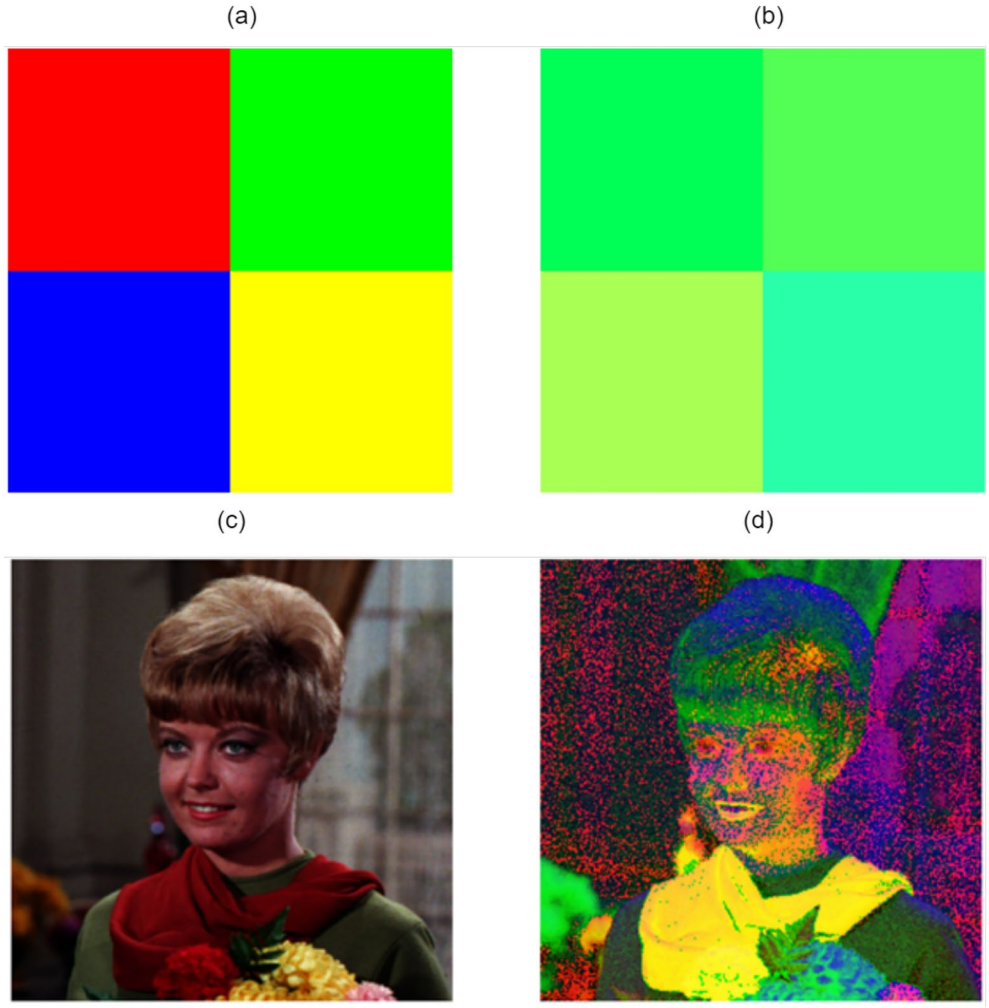

Fig. 8. (**a**, **c**) Original RGB image[47] and (**b**, **d**) HSI image.

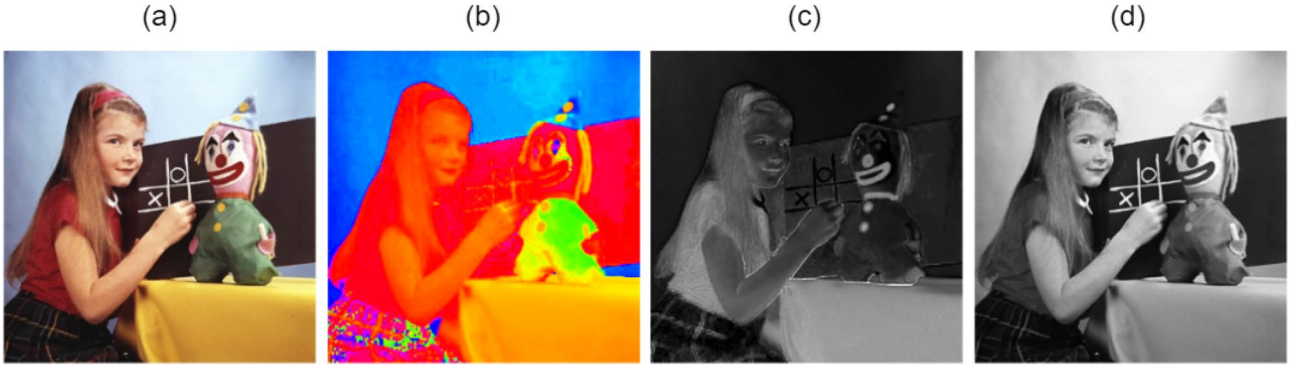

Fig. 9. (**a**) Carole Hersee[48] and the corresponding (**b**) *H*, (**c**) *S*, and (**d**) *I* components.

where A and B are the RGB vectors of two pixels, and denotes the dot product.

Image representation: quantum pixel via Fourier transformation

All quantum pixels of discrete images can be formulated as digital images, which may be either greyscale or coloured. The difference lies in the fact that coloured images are represented in three channels: red (R), green (G), and blue (B), whereas a greyscale image is represented by just the red channel. Each pixel is defined by its coordinates (x, y) and a value between 0 and 255, denoted as $P(x, y)$. A pixel can be defined as a quantum pixel

to work with quantum properties. Since the system operates in a probabilistic space, the pixel's grey value must be normalised to the range [0, 1]. Therefore, the quantum pixel can be formulated as[13]:

$$|P_{x,y}\rangle = \frac{1}{\sqrt{255}}\left(\sqrt{255 - P_{x,y}}|0\rangle + \sqrt{P_{x,y}}|1\rangle\right) \tag{27}$$

where $\frac{1}{\sqrt{255}}$ is the normalisation factor, $\sqrt{255 - P_{x,y}}$ represents the amplitude for the black state ($|0\rangle$), and $\sqrt{P_{x,y}}$ represents the amplitude for the white state ($|1\rangle$).

A quantum state for a pixel is defined as follows:

$$|P_{x,y}\rangle = \cos\theta_{x,y}|0\rangle + \sin\theta_{x,y}|1\rangle. \tag{28}$$

where $\cos\theta_{n,m}$ and $\sin\theta_{n,m}$ are derived from the pixel intensity $P_{x,y}$, and $\theta_{x,y}$ is the angle defined as:

$$\theta_{n,m} = \cos^{-1}\sqrt{1 - \frac{P_{x,y}}{255}}, \tag{29}$$

For an image with $n \times m$ quantum pixels, the superposition state of the entire image requires $(q + p + 1)$ qubits and is defined by the following formula:

$$\begin{aligned} |I\rangle &= \frac{1}{\sqrt{NM}}\sum_{x=0}^{N-1}\sum_{y=0}^{M-1}|P_{x,y}\rangle \otimes |x,y\rangle \\ &= \frac{1}{\sqrt{NM}}\sum_{x=0}^{N-1}\sum_{y=0}^{M-1}(\cos\theta_{x,y}|0\rangle + \sin\theta_{x,y}|1\rangle) \otimes |x,y\rangle \end{aligned} \tag{30}$$

where $q + p$ corresponds to all pixel positions, and one additional qubit is allocated for intensity $P_{x,y}$. The phase factor is defined as:

$$\alpha = \frac{\pi}{2 \times 255} \tag{31}$$

At this stage, Euler's formula is used:

$$e^{i\alpha P_{x,y}} = \cos(\alpha P_n) + i\sin(\alpha P_n) \tag{32}$$

Thus, the intensity of each pixel $P_{x,y}$ is Fourier transformed to the phase representation quantum state, which is defined as:

$$e^{i\alpha P_{x,y}} = e^{i\left(\frac{\pi}{510}\right)P_{x,y}} \tag{33}$$

The quantum state for the entire image is constructed by taking the $\otimes$ tensor product of all pixel states and their corresponding *x*, *y* positions. Therefore, (9) becomes:

$$|I\rangle = \frac{1}{\sqrt{NM}}\sum_{y=0}^{N-1}\sum_{x=0}^{M-1}e^{i\left(\frac{\pi}{510}\right)P_{x,y}}|x,y\rangle \tag{34}$$

For example, consider a 2×2 image with pixel intensities $(P_{0,0}, P_{0,1}, P_{1,0}, P_{1,1}) = (100, 150, 200, 250)$. The quantum states for each pixel are represented as follows:

$$|I\rangle = \frac{1}{2}\left(e^{i\frac{100\pi}{55\pi}}|00\rangle + e^{i\frac{150\pi}{510}}|01\rangle + e^{i\frac{200\pi}{510}}|10\rangle + e^{i\frac{250\pi}{510}}|11\rangle\right) \tag{35}$$

It can be observed that a single qubit can represent the pixel intensity $P_{x,y}$ using $e^{i\alpha P_{x,y}}$.

Proposed quantum image representation and preparation

A new model for quantum image representation in the HSI colour space, based on adjacency information and the adjacency Fourier transform, called Fourier quantum image representation of HSI (AFQIRHSI), is introduced in this paper. This section provides a comprehensive explanation of the AFQIRHSI model and the detailed process of converting classical images into the FQIRHSI format.

While models such as QIRHSI and EQIRHSI encode the H and S information of each image pixel using two superposition qubits and entangled qubits, respectively, the AFQIRHSI model encodes H and S information for each pixel using two entangled qubits. Additionally, it uses two qubits to represent the entanglement between adjacency information and pixel intensity. This approach enables the classical image to be accurately and efficiently retrieved from the AFQIRHSI quantum system through quantum measurement. Figure 10 illustrates

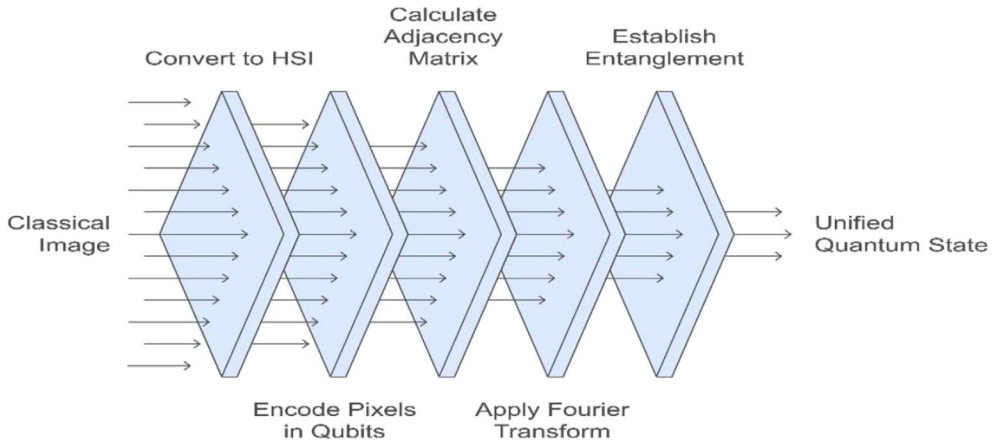

Fig. 10. Layers of AFQIRHSI procedures.

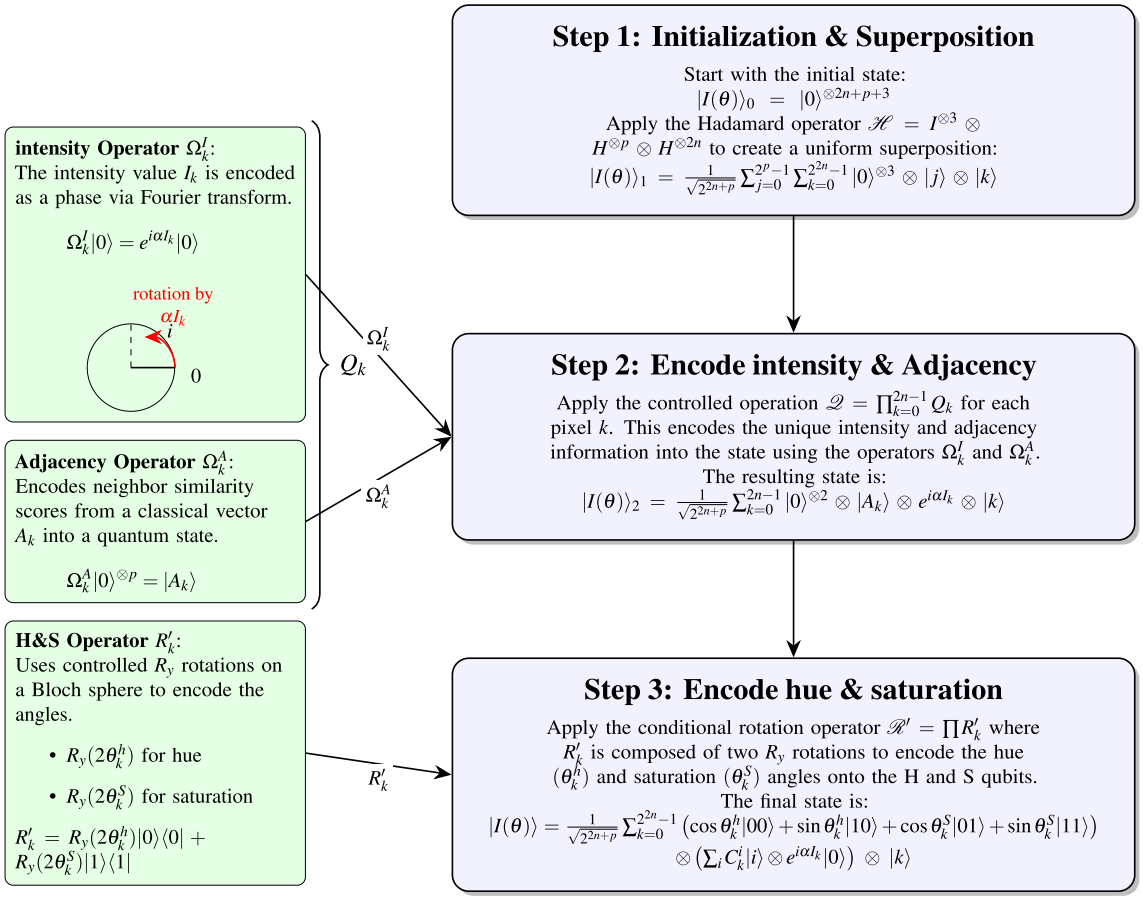

Fig. 11. Steps to generate the AFQIRHSI model.

the layers of the AFQIRHSI procedure, while Fig. 11 outlines the steps to generate AFQIRHSI. Figure 12 and Eq. ?? (missing number of Eq. which is below Eq. 39 should move under figure 12, and not related to Theorem 1) illustrate an example of a 2×2 image and its representation using AFQIRHSI, , while Fig. 13 outlines the corresponding quantum circuit and Fig. 14 illustrates the quantum circuit for $n = 2$ in the AFQIRHSI representation, implemented using the Qiskit library.

Theorem 1 Suppose we have 2^{2n} sequences of Fourier transform $e^{i\alpha I_m}$, $\left(m = 0, 1, \ldots 2^{2n} - 1\right)$, where $\alpha = 2\pi/1024$ and I_m values and two vectors of angles $\left\{\theta_k^h, \theta_k^S\right\} \in \left[0, \frac{\pi}{2}\right]$. There exists a unitary transform Q

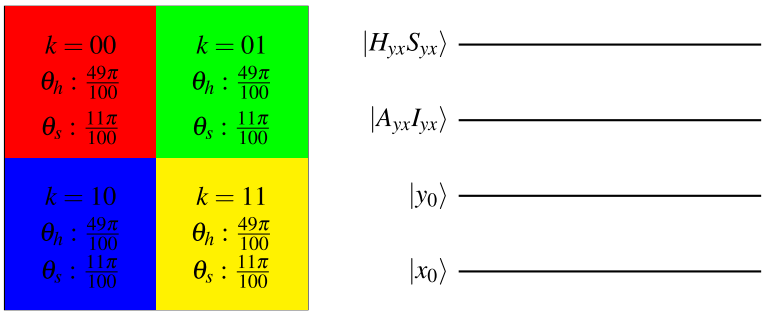

Fig. 12. Example of a 2×2 image, its representation using AFQIRHSI, and its corresponding quantum circuit, respectively.

that converts quantum computers from the initialised state $|0\rangle^{\otimes 2n+p+3}$ to the AFQIRHSI state $|I(\theta)\rangle$, which is composed of Hadamard, controlled-not, and controlled-rotation transformations.

$$|I(\theta)\rangle = \frac{1}{\sqrt{2^{2n+p}}} \sum_{k=0}^{2^{2n}-1} \left(\cos\theta_k^h|00\rangle + \sin\theta_k^h|10\rangle + \cos\theta_k^S|01\rangle + \sin\theta_k^S|11\rangle\right) \otimes \left(\sum_i C_k^i|i\rangle \otimes e^{i\alpha I_k}|0\rangle\right) \otimes |k\rangle \quad (36)$$

Proof Step 1. Initialization: Start with the initial state

$$|I(\theta)\rangle_0 = |0\rangle^{\otimes 2n+p+3} \quad (37)$$

where $2n$ qubits represent the position state, $p = 4$ is used for adjacency information, and one qubit is concerned with the intensity value using Fourier transformation.

Hadamard Transformation: By applying $\mathscr{H}$, we have

$$\mathscr{H} = I^{\otimes 3} \otimes H^{\otimes p} \otimes H^{\otimes 2n} \quad (38)$$

where

$$I = \begin{pmatrix} 1 & 0 \\ 0 & 1 \end{pmatrix}, \mathrm{H} = \begin{pmatrix} \frac{1}{\sqrt{2}} & \frac{1}{\sqrt{2}} \\ \frac{1}{\sqrt{2}} & \frac{-1}{\sqrt{2}} \end{pmatrix} \quad (39)$$

$$\begin{aligned}
&|I(\theta)\rangle \\
&= \frac{1}{2\sqrt{2}}\Bigg[\left(\cos\left(\frac{49\pi}{100}\right)|00\rangle + \sin\left(\frac{49\pi}{100}\right)|10\rangle + \cos\left(\frac{11\pi}{100}\right)|01\rangle + \sin\left(\frac{11\pi}{100}\right)|11\rangle\right) \otimes \left(\frac{1}{\sqrt{2}}|0\rangle \otimes |0\rangle + \frac{1}{\sqrt{2}}|1\rangle \otimes |0\rangle\right) \otimes |00\rangle \\
&+ \left(\cos\left(\frac{49\pi}{100}\right)|00\rangle + \sin\left(\frac{49\pi}{100}\right)|10\rangle + \cos\left(\frac{11\pi}{100}\right)|01\rangle + \sin\left(\frac{11\pi}{100}\right)|11\rangle\right) \otimes \left(\frac{1}{\sqrt{2}}|0\rangle \otimes |0\rangle + \frac{1}{\sqrt{2}}|1\rangle \otimes |0\rangle\right) \otimes |01\rangle \\
&+ \left(\cos\left(\frac{49\pi}{100}\right)|00\rangle + \sin\left(\frac{49\pi}{100}\right)|10\rangle + \cos\left(\frac{11\pi}{100}\right)|01\rangle + \sin\left(\frac{11\pi}{100}\right)|11\rangle\right) \otimes \left(\frac{1}{\sqrt{2}}|0\rangle \otimes |0\rangle + \frac{1}{\sqrt{2}}|1\rangle \otimes |0\rangle\right) \otimes |10\rangle \\
&+ \left(\cos\left(\frac{49\pi}{100}\right)|00\rangle + \sin\left(\frac{49\pi}{100}\right)|10\rangle + \cos\left(\frac{11\pi}{100}\right)|01\rangle + \sin\left(\frac{11\pi}{100}\right)|11\rangle\right) \otimes \left(\frac{1}{\sqrt{2}}|0\rangle \otimes |0\rangle + \frac{1}{\sqrt{2}}|1\rangle \otimes |0\rangle\right) \otimes |11\rangle\Bigg].
\end{aligned}$$

By applying $\mathscr{H}$ on $|I(\theta)\rangle_0$, we obtain

$$\begin{aligned}
\mathscr{H}|0\rangle^{\otimes 2n+p+3} &= \left(I^{\otimes 3} \otimes H^{\otimes p} \otimes H^{\otimes 2n}\right)|0\rangle^{\otimes 2n+p+3} \\
|I(\theta)\rangle_1 &= \frac{1}{\sqrt{2^{2n+p}}} \sum_{j=0}^{2^p-1} \sum_{k=0}^{2^{2n}-1} |0\rangle^{\otimes 3} \otimes |j\rangle \otimes |k\rangle
\end{aligned} \quad (40)$$

Step 2. In this step, we store the intensity and adjacency information for each pixel. We need to apply a quantum suboperation Q_m on each of the 2^{2n} pixels, defined as:

$$Q_m = I^{\otimes(2n+p+3)} \otimes \sum_{k \neq m} |k\rangle\langle k| + \left(\Omega_m^I \otimes \Omega_m^A - I^{\otimes(2n+p+3)}\right) \otimes |m\rangle\langle m| \quad (41)$$

The suboperation Q_m is applied to both the Fourier transform-based intensity encoding and the adjacency matrix encoding for the m-th pixel.

Where Ω_m^I is a quantum operation that applies the Fourier transform to encode the intensity value for pixel m :

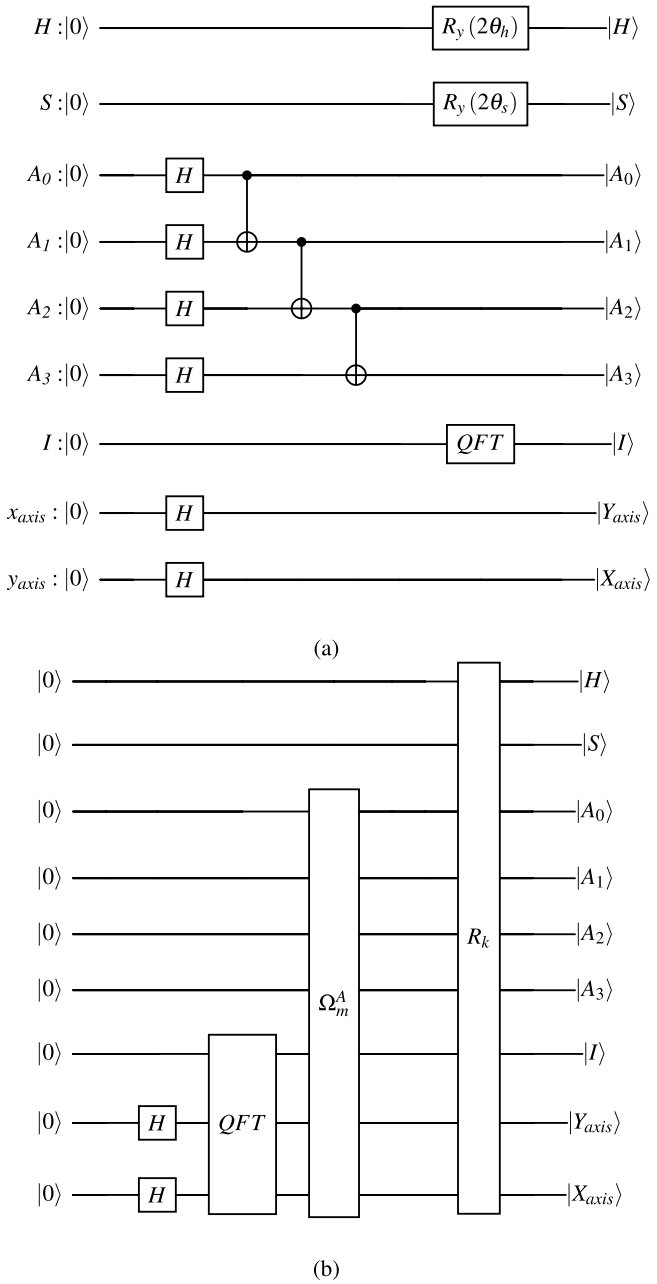

Fig. 13. (**a**) Quantum circuit for the AFQIRHSI representation of the pixel at position $(0, 0)$ from the image in Fig. 12, (**b**) Detailed quantum circuit operations for AFQIRHSI.

$$\Omega_m^I|0\rangle = e^{i\alpha I_m}|0\rangle = |I_{\mathrm{m}}\rangle \tag{42}$$

and Ω_m^A is the quantum operation used to encode the adjacency information of pixel m :

$$\Omega_m^A|0\rangle = |A_m\rangle \tag{43}$$

Each element in A_m represents the similarity score with neighbouring pixels. The adjacency vector can be defined as:

If $p = 4$ then $A_m = \left(C_m^0, C_m^1, C_m^2, C_m^3\right)$.

If $p = 8$ then $A_m = \left(C_m^0, C_m^1, C_m^2, C_m^3, C_m^4, C_m^5, C_m^6, C_m^7\right)$.

Where C_m^{i}, for $i = 1, \ldots, p$, refers to the similarity with a neighbouring pixel. For example, let pixel m have the following information:

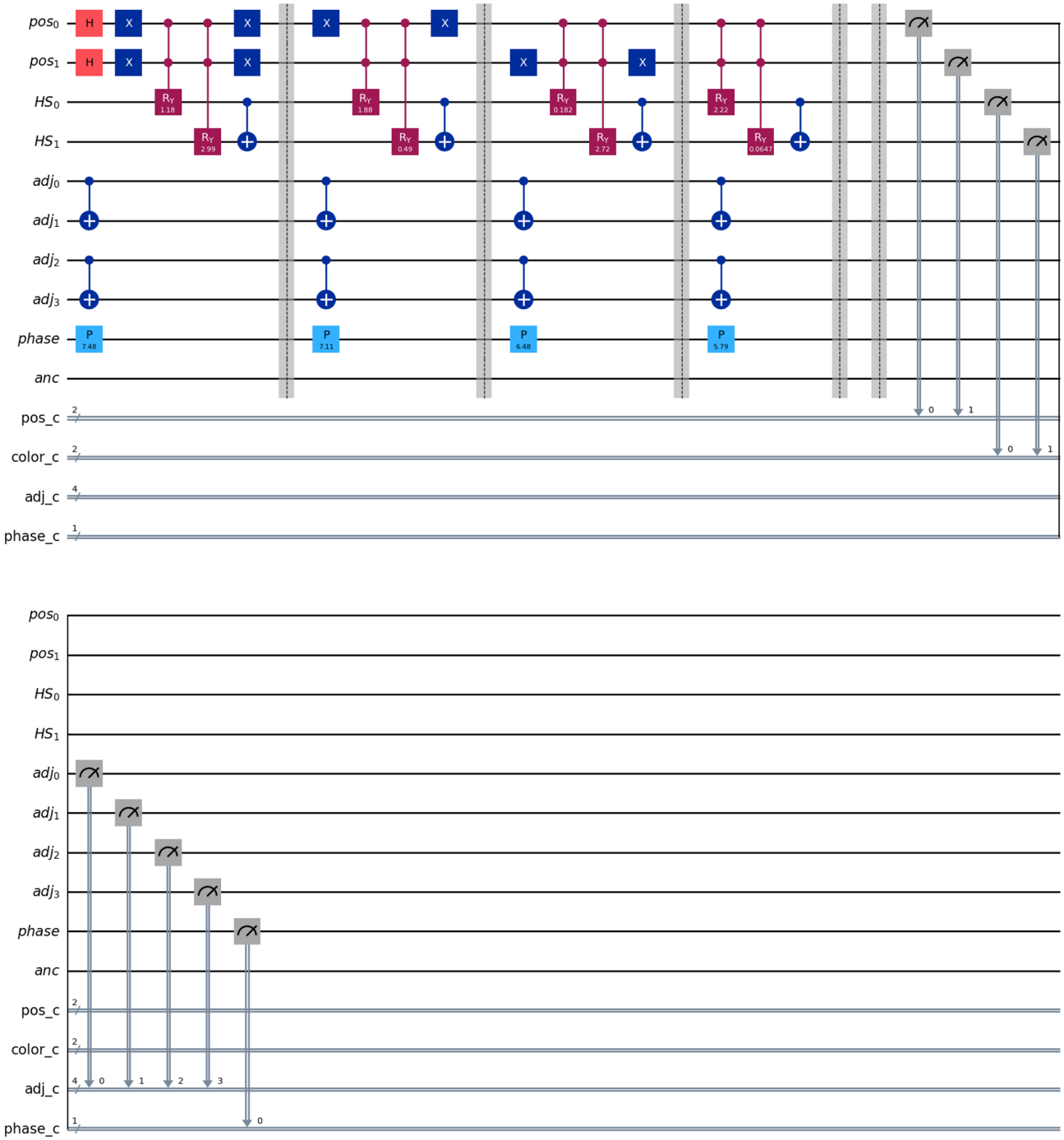

Fig. 14. Quantum circuit for $n = 2$ in the AFQIRHSI representation.

$$A_m = \left(C_m^0, C_m^1, C_m^2, C_m^3\right) = (\text{ up }, \text{ down}, \text{ left }, \text{ righ }) = (0.8, 0.3, 0.7, 0.9)$$

This can be expressed as a quantum state:

$$|A_m\rangle = C_m^0|0\rangle + C_m^1|1\rangle + C_m^2|2\rangle + C_m^3|3\rangle \tag{44}$$

The value 0.8 represents the high similarity between pixel m and the 'up' pixel, 0.3 indicates low similarity between pixel m and 'down' pixel, and so on. The quantum XOR operation is applied if $p = 4$, meaning four qubits are used to encode adjacency information for each pixel m :

$$\Omega_m^A|0\rangle^{\otimes p} = \otimes_{i=0}^{p-1}\left(\left|0 \oplus C_m^i\right\rangle\right) = \left|C_m^0\right\rangle\left|C_m^1\right\rangle\left|C_m^2\right\rangle\left|C_m^3\right\rangle \tag{45}$$

In general, the operation can be written as:

$$\Omega_m^A|0\rangle^{\otimes p} = \otimes_{i=0}^{p-1}\left|C_m^i\right\rangle = |A_m\rangle \tag{46}$$

Thus Ω_m^A is a unitary operation, which can be expressed as:

$$\Omega_m^A = \otimes_{i=0}^{p-1}\,\mathrm{CNOT}\left(C_m^i\right) \tag{47}$$

Where gate CNOT $\left(C_m^i\right)$ flips the i-th qubit if $C_m^i = 1$.

Next, applying the suboperation Q_m on $|I(\theta)\rangle_1$, we obtain:

$Q_m|I(\theta)\rangle_1 = \frac{1}{\sqrt{2^{2n+p}}}\left(\sum_{j=0}^{2^p-1}\sum_{k\neq m}^{2^{2n}-1}|0\rangle^{\otimes 3}\otimes|j\rangle\otimes|k\rangle + \sum_{j=0}^{2^p-1}|0\rangle^{\otimes 2}\otimes|A_m\rangle\otimes e^{i\alpha I_m}|0\rangle\otimes|m\rangle\right)$

If we apply Q to two different pixels m and s, for example Q_sQ_m on $|I(\theta)\rangle_1$, we obtain:

$$Q_sQ_m|I(\theta)\rangle_1 = \frac{1}{\sqrt{2^{2n+p}}}\left(\sum_{k\neq m,s}|0\rangle^{\otimes 3}\otimes\sum_{l=0}^{1}|l\rangle\otimes|0\rangle^{\otimes p}\otimes|k\rangle + \sum_{j=0}^{2^p-1}|0\rangle^{\otimes 2}\otimes|A_m\rangle\otimes e^{i\alpha I_m}|0\rangle\otimes\right. \tag{48}$$

$$\left.|m\rangle + \sum_{j=0}^{2^p-1}|0\rangle^{\otimes 2}\otimes|A_s\rangle\otimes e^{i\alpha I_s}|0\rangle\otimes|s\rangle\right) \tag{49}$$

For three different pixels m, s, and r, we get:

$$Q_rQ_sQ_m|I(\theta)\rangle_1 = \frac{1}{\sqrt{2^{2n+p}}}\left(\sum_{k\neq m,s,r}|0\rangle^{\otimes 3}\otimes\sum_{l=0}^{1}|l\rangle\otimes|0\rangle^{\otimes p}\otimes|k\rangle + \sum_{j=0}^{2^p-1}|0\rangle^{\otimes 2}\otimes|A_m\rangle\otimes e^{i\alpha I_m}\mid 0\right.$$
$$\left.\otimes|m\rangle + \sum_{j=0}^{2^p-1}|0\rangle^{\otimes 2}\otimes|A_s\rangle\otimes e^{i\alpha I_s}|0\rangle\otimes|s\rangle\right) + \sum_{j=0}^{2^p-1}|0\rangle^{\otimes 2}\otimes|A_r\rangle\otimes e^{i\alpha I_r}|\rangle\otimes|r\rangle\Bigg) \tag{50}$$

and

$$\mathscr{Q} = \prod_{k=0}^{2n-1}Q_k \tag{51}$$

In general, we have

$$|I(\theta)_2\rangle = \prod_{k=0}^{2n}-1 \tag{52}$$

$$Q|I(\theta)\rangle_1$$
$$|I(\theta)\rangle_2 = \frac{1}{\sqrt{2^{2n+p}}}\sum_{k=0}^{2n-1}|0\rangle^{\otimes 2}\otimes|A_k\rangle\otimes e^{i\alpha I_k}\otimes|k\rangle \tag{53}$$

At this stage, to entangle the A_k with the I_k, we apply a controlled phase rotation $CR_z\,(\alpha I_k)$. The $CR_z(\alpha)$ is a quantum gate that applies a phase rotation $R_z(\alpha)$ to a k-th qubit, defined as:

$$R_z(\alpha) = \begin{pmatrix} e^{-i\alpha/2} & 0 \\ 0 & e^{i\alpha/2} \end{pmatrix} \tag{54}$$

The $CR_z\,(\alpha I_k)$ can be expressed as:

$$CR_z\,(\alpha I_k) = I\otimes|0\rangle\langle 0| + R_z(\alpha)\otimes|1\rangle\langle 1| \tag{55}$$

Now, we apply $CR_z\,(\alpha I_k)$ to entangle the A_k with the I_k, obtaining:

$$CR_z\,(\alpha I_k)\left(\sum_i C_k^i|i\rangle\otimes|0\rangle\right) = \sum_i C_k^i|i\rangle\otimes e^{i\alpha I_k}|0\rangle \tag{56}$$

Then,

$$|I(\theta)\rangle_2 = \frac{1}{\sqrt{2^{2n+p}}} \sum_{k=0}^{2n-1} |0\rangle^{\otimes 2} \otimes \sum_i C_k^i |i\rangle \otimes e^{i\alpha I_k} |0\rangle \otimes |k\rangle \tag{57}$$

Step 3 To encode the H and S, we use rotation matrices around the y-axis of the Bloch sphere. H can be represented as an angle and can be encoded as a phase in a quantum state. To encode the hue H_i :

$$H_i \to R_y(2\theta_i) = \begin{pmatrix} \cos\theta & -\sin\theta \\ \sin\theta & \cos\theta \end{pmatrix}, \theta \in \left\{\theta_i^h\right\} \tag{58}$$

The S can be encoded as an amplitude. One approach is to use the R_y gate to encode these values:

$$S_i \to R_y(2\theta_i) = \begin{pmatrix} \cos\theta & -\sin\theta \\ \sin\theta & \cos\theta \end{pmatrix} \theta \in \{\theta_i^s\} \tag{59}$$

In this step, we design two control rotation matrices, R_i^h and R_i^S, to apply specific rotations around the y axis of the Bloch sphere based on the state of a control qubit. The matrix R_i^h applies the rotation $R_y\left(2\theta_i^h\right)$ when the control qubit is in the state $|0\rangle$, while the identity operation I is applied when the control qubit is in the state $|1\rangle$, meaning no rotation occurs. The matrix R_k^S applies the rotation $R_y\left(2\theta_i^S\right)$ when the control qubit is in the state $|1\rangle$, and the identity operation I is applied when the control qubit is in the state $|0\rangle$, meaning no rotation occurs.

At this stage, it is important to construct R_i^h. We need to ensure that the rotation $R_y\left(2\theta_i^h\right)$ is applied when the control qubit is $|0\rangle$, and the identity operation I is applied when the control qubit is $|1\rangle$.

For the rotation when the control qubit is in the state $|0\rangle$, we apply $R_y\left(2\theta_i^h\right)$, yielding:

$$R_y\left(2\theta_i^h\right) \otimes |0\rangle\langle 0| \tag{60}$$

For the rotation when the control qubit is in the state $|1\rangle$, we apply the identity operation, yielding:

$$I \otimes |1\rangle\langle 1|. \tag{61}$$

From (59) and (60), the control rotation matrix R_k^h is given by:

$$R_i^h = I \otimes |1\rangle\langle 1| + R_y\left(2\theta_i^h\right) \otimes |0\rangle\langle 0| \tag{62}$$

Alternatively, this can be written as:

$$R_i^h = \begin{pmatrix} R_y\left(2\theta_i^h\right) & 0 \\ 0 & I \end{pmatrix} \tag{63}$$

Similarly, to construct R_i^S, we need to ensure that the rotation $R_y\left(2\theta_i^S\right)$ is applied when the control qubit is in the state $|1\rangle$, and the identity operation I is applied when the control qubit is in the state $|0\rangle$

We have,

$$R_i^S = I \otimes |0\rangle\langle 0| + R_y\left(2\theta_k^S\right) \otimes |1\rangle\langle 1| \tag{64}$$

Alternatively, this can be written as:

$$R_i^S = \begin{pmatrix} I & 0 \\ 0 & R_y\left(2\theta_k^S\right) \end{pmatrix} \tag{65}$$

It is necessary to apply a unitary transform R_k, where $k = 0, 1, \ldots, 2_{2n} - 1$, since R_k is a unitary transformation, meaning $R_k R_k^\dagger = I^{\otimes 2n+p+3}$.

To encode the angle of $H\left(\theta_k^h\right)$ and the angle of $S\left(\theta_k^S\right)$ into the quantum state, we apply controlled rotations based on the state of the qubits. We multiply R_k^h and R_k^s, as it is necessary to apply these rotations conditionally based on the state of the target qubit. This gives the operation as follows:

$$R_k' = R_k^h R_k^s \tag{66}$$

In our conditional rotations, R_k^h applies the rotation $R_y\left(2\theta_k^h\right)$ when the target qubit is in the state $|0\rangle$, and R_k^S applies the rotation $R_y\left(2\theta_k^S\right)$ when the target qubit is in the state $|1\rangle$.

The result of the multiplication of R_k^h and R_k^S is given by:

$$R'_k = \begin{pmatrix} I & 0 \\ 0 & R_y\left(2\theta_k^S\right) \end{pmatrix} \begin{pmatrix} R_y\left(2\theta_k^h\right) & 0 \\ 0 & I \end{pmatrix}.$$

$$R'_k = \begin{pmatrix} I \cdot R_y\left(2\theta_k^h\right) + 0 \cdot 0 & I \cdot 0 + 0 \cdot I \\ 0 \cdot R_y\left(2\theta_k^h\right) + R_y\left(2\theta_k^S\right) \cdot 0 & 0 \cdot 0 + R_y\left(2\theta_k^S\right) \cdot I \end{pmatrix},$$

$$R'_k = \begin{pmatrix} R_y\left(2\theta_k^h\right) & 0 \\ 0 & R_y\left(2\theta_k^S\right) \end{pmatrix}.$$

and can expressed as:

$$R'_k = R_y\left(2\theta_k^h\right) \otimes |0\rangle\langle 0| + R_y\left(2\theta_k^S\right) \otimes |1\rangle\langle 1|. \tag{67}$$

By applying R_k to $|I(\theta)\rangle_2$, we obtain:

For simplicity, let us define:

$$|A_k\rangle \otimes e^{i\alpha I_k} = \left(\sum_i C_k^i |i\rangle \otimes e^{i\alpha I_k}|0\rangle\right) \tag{68}$$

$$\begin{aligned} R_k|I(\theta)\rangle_2 &= \left\{ I^{\otimes 2} \otimes \sum_{j=0, j\neq k}^{2^{2n}-1} |j\rangle\langle j| + \left(R_y\left(2\theta_k^h\right) \otimes |0\rangle\langle 0| + R_y\left(2\theta_k^s\right) \otimes |1\rangle\langle 1|\right) \otimes |k\rangle\langle k| \right\} \\ &\times \frac{1}{\sqrt{2^{2n+p}}} \sum_{k=0}^{2^{2n}-1} |0\rangle^{\otimes 2} \otimes \sum_{l=0}^{1} |l\rangle \otimes |A_k\rangle \otimes e^{i\alpha I_k} \otimes |k\rangle \\ &= \frac{1}{\sqrt{2^{2n+p}}} \left\{ \sum_{j\neq k} |0\rangle \otimes \sum_{l=0}^{1} |l\rangle \otimes |A_j\rangle \otimes e^{i\alpha I_j} \otimes |j\rangle + |0\rangle \otimes \sum_{l=0}^{1} |l\rangle \otimes R'_k\,|A_k\rangle \otimes e^{i\alpha I_k} \otimes |k\rangle \right\} \end{aligned} \tag{69}$$

where $R'_k\,|A_k\rangle$ can be expanded as:

$$\begin{aligned} R'_k\,|A_k\rangle &= \left(R_y\left(2\theta_k^h\right) \otimes |0\rangle\langle 0| + R_y\left(2\theta_k^S\right) \otimes |1\rangle\langle 1|\right)|A_k\rangle \\ R'_k\,|A_k\rangle &= \cos\left(\theta_k^h\right)|0\rangle \otimes |0\rangle + \sin\left(\theta_k^h\right)|1\rangle \otimes |0\rangle + \cos\left(\theta_k^S\right)|0\rangle \otimes |1\rangle + \sin\left(\theta_k^S\right)|1\rangle \otimes |1\rangle \end{aligned} \tag{70}$$

Therefore:

$$\begin{aligned} R_k|I(\theta)\rangle_2 =& \frac{1}{\sqrt{2^{2n+p}}} \left\{ \sum_{j\neq k} |0\rangle \otimes \sum_{l=0}^{1} |l\rangle \otimes |A_j\rangle \otimes e^{i\alpha I_j} \otimes |j\rangle \right. \\ &\left. + \left(\cos\theta_k^h|00\rangle + \sin\theta_k^h|10\rangle + \cos\theta_k^s|01\rangle + \sin\theta_k^s|11\rangle\right) \otimes |A_k\rangle \otimes e^{i\alpha I_k} \otimes |k\rangle \right\}. \end{aligned} \tag{71}$$

Next, applying $R_m R_k$ on $|I(\theta)\rangle_2$, we obtain:

$$\begin{aligned} R_m R_k|I(\theta)\rangle_2 =& \frac{1}{\sqrt{2^{2n+p}}} \left\{ \sum_{j\neq k,m} |0\rangle \otimes \sum_{l=0}^{1} |l\rangle \otimes |A_j\rangle \otimes e^{i\alpha I_j} \otimes |j\rangle \right. \\ &+ \left(\cos\theta_k^h|00\rangle + \sin\theta_k^h|10\rangle + \cos\theta_k^s|01\rangle + \sin\theta_k^s|11\rangle\right) \otimes |A_k\rangle \otimes e^{i\alpha I_k} \otimes |k\rangle \\ &\left. + \left(\cos\theta_m^h|00\rangle + \sin\theta_m^h|10\rangle + \cos\theta_m^s|01\rangle + \sin\theta_m^s|11\rangle\right) \otimes |A_m\rangle \otimes e^{i\alpha I_m} \otimes |m\rangle \right\} \end{aligned} \tag{72}$$

Finally, for all R_k, we have:

$$R|I(\theta)\rangle_2 = \left(\prod_{k=0}^{2n-1} R_k\right)|I(\theta)\rangle_2 \tag{73}$$

$$R|I(\theta)\rangle_2 = \frac{1}{\sqrt{2^{2n+1}}} \sum_{k=0}^{2^{2n}-1} \left(\cos\theta_k^h|00\rangle + \sin\theta_k^h|10\rangle + \cos\theta_k^s|01\rangle + \sin\theta_k^s|11\rangle\right) \otimes |A_k\rangle \otimes e^{i\alpha I_k} \otimes |k\rangle \tag{74}$$

The final state $|I(\theta)\rangle$, which includes H, S, A_k, and I_k based on $e^{i\alpha I_k}$, is represented as:

$$|I(\theta)\rangle = \frac{1}{\sqrt{2^{2n+p}}} \sum_{k=0}^{2^{2n}-1} \left(\cos\theta_k^h|00\rangle + \sin\theta_k^h|10\rangle + \cos\theta_k^S|01\rangle + \sin\theta_k^S|11\rangle\right)$$
$$\otimes \left(\sum_i C_k^i|i\rangle \otimes e^{i\alpha I_k}|0\rangle\right) \otimes |k\rangle$$

Therefore, when the unitary transform $\mathscr{M} = RQH$ is applied, we can obtain $|I(\theta)\rangle$. This proof involves the use of several gates, including Hadamard (H), NOT, and CNOT gates.

The implementation of the unitary transform *M* as outlined in Theorem 1 is carried out in three steps: *H*, *Q*, and *R*. In step 1, *H* requires $2n + p$ Hadamard gates and 3 identity gates. In step 2, *Q* involves constructing $(p.n + 1) \cdot 2^{2n}$ controlled-NOT gates. In the last step, *R* needs 2^{2n} controlled-NOT gates.□

Note in the AFQIRHSI model, the operation *H* in step 1 involves a number of operations equal to $2n + \mathrm{p}$. In step *Q*, which prepares the intensity value I_k and adjacency information, the required operations are *pn* for intensity and *pn* for the adjacency matrix information. Since *Q* has two suboperations, Ω_m^I for intensity and Ω_m^A for the adjacency matrix, each using a controlled gate $CR_z(\alpha I_k)$, the total number of operations for *Q* is $(p.n + 1) \cdot 2^{2n}$. In the last step, the rotation transformation *R* involves 2^{2n} operations, given by $R = \prod_{k=0}^{2^{2n-1}} R_k$.

Since each R_k includes $C^{2n+1}\left(R_y\left(\frac{2\theta_k^h}{2^{2n}-1}\right)\right)$ and $C^{2n+1}\left(R_y\left(\frac{2\theta_k^s}{2^{2n}-1}\right)\right)$ gates (from Eqs. () and ()), $C^{2n+1}\left(R_y\left(\frac{2\theta_k^h}{2^{2n}-1}\right)\right.$ can be broken down into $2^{2n+1} - 1$ elementary gates (for $R_y\left(\frac{2\theta_k^h}{2^{2n}-1}\right)$ and $R_y\left(\frac{2\theta_k^s}{2^{2n}-1}\right)$), as well as $2^{2n+1} - 2$ CNOT gates.

Considering this analysis, for a $2^n \times 2^n$ colour image, we need $2n + p$ Hadamard gates, less than $(p.n+ 1) \cdot 2^{2n}$ CNOT gates, $2 \times 2^{2n} \times \left(2^{2n} - 1\right)$ rotation gates, and $2 \times 2^{2n} \times \left(2^{2n} - 2\right)$ CNOT gates to prepare the AFQIRHSI state. The complexity of preparing the AFQIRHSI state is thus given by:

$$\begin{aligned} &O\left(2n + p + p(n+1) \cdot 2^{2n} + 2 \times 2^{2n} \times \left(2^{2n+1} - 1 + 2^{2n+1} - 2\right)\right) \\ &= O\left(2n + p + (p-5) \cdot 2^{2n} + 4 \cdot 2^{4n}\right) \end{aligned} \tag{75}$$

For $p = 4$, this simplifies to:

$$O\left(2n + 4 - 2^{2n} + 4 \cdot 2^{4n}\right)$$

Quantum image colour operations

In this section, we introduce several quantum colour image processing operations on AFQIRHSI, including complement colour transformation and position operations. Additionally, quantum circuits are designed for each corresponding operation.

Complement colour transformation U_{cc}

The U_{cc} is a quantum operation that transforms the colour of a pixel to its complementary colour. In the field of QIP, this transformation is applied to the quantum state representing the colour information of the image.

The unitary operator U_{cc} can be defined as:

$$U_{cc}|\psi\rangle = \left|\psi'\right\rangle \tag{76}$$

where $|\psi'\rangle$ is the quantum state representing the complementary colour.

In mathematical terms, *H* is transformed into its complementary value H', which is given by $H' = (H + 180^\circ) \bmod 360^\circ$, meaning *H* should be shifted by 180 degrees. To achieve this, we use a rotation gate to adjust *H*, which is defined as:

$$R_z(\theta) = \begin{pmatrix} e^{-i\theta/2} & 0 \\ 0 & e^{i\theta/2} \end{pmatrix} \tag{77}$$

The $R_z(\theta)$ applies a phase shift of θ radians (180 degrees) to the *H* component.

To reflect the complementary colour, the *S* undergoes an inversion operation, mathematically represented as:

$$S' = 1 - S \tag{78}$$

We use the rotation gate $R_y(\pi)$ to adjust the saturation: $R_y(\pi) = \begin{pmatrix} \cos(\pi/2) & -\sin(\pi/2) \\ \sin(\pi/2) & \cos(\pi/2) \end{pmatrix}$

We apply R_y to the *S* state, as we need to rotate the value of *S* by an angle that transforms the saturation to its complementary value.

For *I*, it should be transformed as $255 - I_k$, i.e. $I'_k = 255 - I_k$.

Since A_k primarily encodes the relationships between pixels and does not directly relate to the colour information, it does not affect the U_{cc} operation.

Thus, the U_{cc} can be represented as:

$$U_{cc} = U_H \otimes U_S \otimes U_I \tag{79}$$

where U_H is the unitary operator that transforms the H to its complementary value, and (U_S, U_I) are unitary operators acting on the saturation and intensity values, respectively. Figure 15 (a) shows the U_{cc} process. We apply U_{cc} on $|I\rangle$. In the first step, we apply $R_z(\pi)$ to the $|H\rangle$, which gives:

$$R_z(\pi)|H\rangle = R_z(\pi)\left(\cos\theta_k^h|00\rangle + \sin\theta_k^h|10\rangle\right) = \cos\left(\theta_k^h + \pi\right)|00\rangle + \sin\left(\theta_k^h + \pi\right)|10\rangle$$

Next, we apply $R_y(\pi)$ to the $|S\rangle$, resulting in:

$$R_y(\pi)|S\rangle = R_y(\pi)\left(\cos\theta_k^S|01\rangle + \sin\theta_k^S|11\rangle\right) = \cos\left(\theta_k^S + \pi\right)|01\rangle + \sin\left(\theta_k^S + \pi\right)|11\rangle$$

For I', we use a classical operation:

$$I' = 255 - I \tag{80}$$

which is simply a change in the I_k value. Therefore, $|I'\rangle$ becomes:

$$\begin{aligned}\left|I'\right\rangle = \frac{1}{\sqrt{2^{2n+1}}}\sum_{k=0}^{2^{2n}-1}&\left(\cos\left(\theta_k^h + 180^\circ\right)|00\rangle + \sin\left(\theta_k^h + 180^\circ\right)|10\rangle + \cos\left(\theta_k^s + 180^\circ\right)|01\rangle + \sin\left(\theta_k^s + \right.\right.\\ &\left.\left.180^\circ\right)|11\rangle\right) \otimes |A_k\rangle \otimes \left|e^{i\alpha(255-I_k)}\right\rangle \otimes |k\rangle\end{aligned} \tag{81}$$

Global colour transformations (G_{ct})

G_{ct} refers to operations that adjust the colour properties of an entire image in a consistent manner, such as brightness adjustment, contrast enhancement, and hue rotation, among others.

Brightness and contrast adjustment is a technique in image processing used to enhance the visual quality of an image. Brightness refers to the overall lightness or darkness of an image. Adjusting the brightness changes the intensity of all the pixels in an image by adding or subtracting a constant value to or from each pixel's intensity. The brightness adjustment is defined as follows:

$$I'_k = I_k + \Delta I \tag{82}$$

where $I(x, y)$ is the original pixel intensity at the position (x, y), and ΔI is the constant added to each pixel to adjust the brightness.

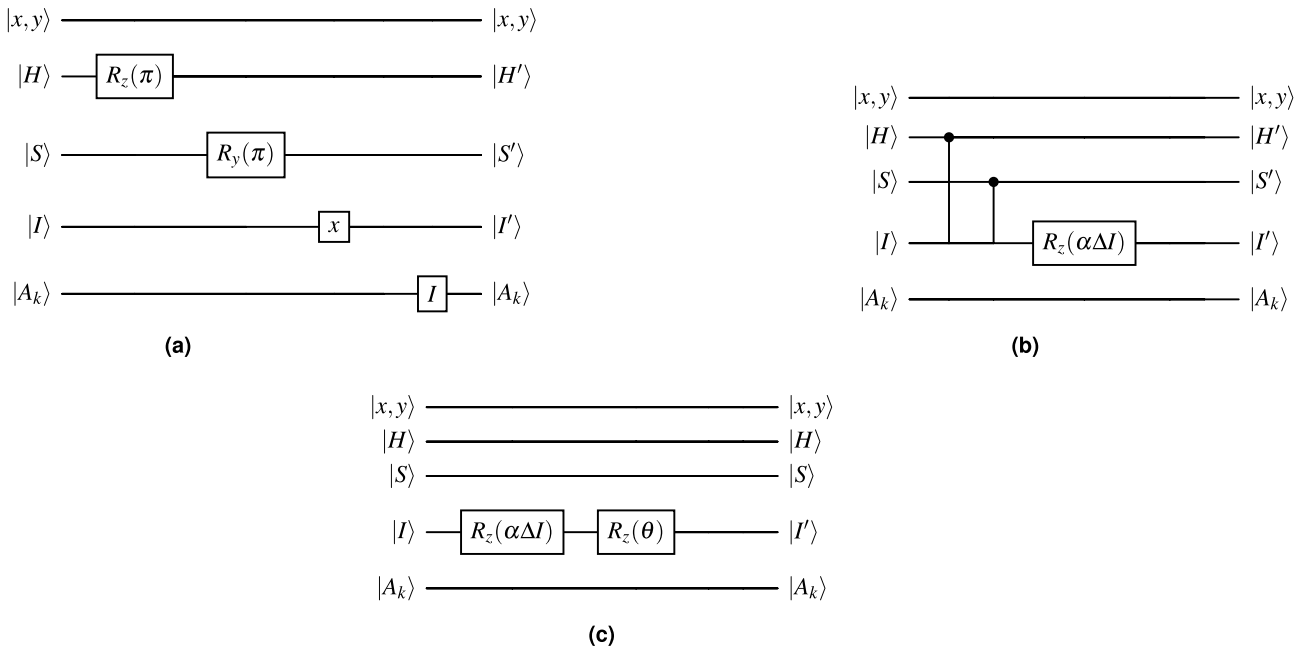

Fig. 15. Quantum circuit diagrams: (**a**) U_{cc}, (**b**) G_{st}, and (**c**) S_{ct}.

Contrast refers to the difference in luminance or colour that makes an object in an image distinguishable. Adjusting the contrast changes the range of pixel intensities in an image. High contrast makes the bright areas brighter and the dark areas darker, enhancing the details and edges in the image. Low contrast reduces the difference between light and dark areas, resulting in a more uniform and flatter appearance. Contrast adjustment is defined as follows:

$$g_{\mathrm{k}} = \frac{f_{\mathrm{k}} - \min(f)}{\max(f) - \min(f)} \cdot (L-1) \tag{83}$$

where $g(i, j)$ is the output pixel value, $f(i, j)$ is the input pixel value, $\min(f)$ and $\max(f)$ are the minimum and maximum intensity values in the image, respectively, and L is the number of possible intensity levels. In our AFQIRHSI model, we already have the intensity I_k :

$$|I_k\rangle = e^{i\alpha I_k}|0\rangle \tag{84}$$

By applying I'_k on $e^{i\alpha I_k}$, we get:

$$e^{i\alpha I'_k}|0\rangle = e^{i\alpha(I_k+\Delta I)}|0\rangle = e^{i\alpha I_k} \cdot e^{i\alpha \Delta I}|0\rangle$$

We use a controlled phase shift $R_z(\alpha\Delta I)$, which is defined as:

$$R_z(\alpha\Delta I) = \begin{pmatrix} e^{-i\alpha\Delta I/2} & 0 \\ 0 & e^{i\alpha\Delta I/2} \end{pmatrix} \tag{85}$$

Apply the phase shift gate $R_z(\alpha\Delta I)$ to the intensity qubits. After brightness adjustment, $|I\rangle$ becomes:

$$\begin{aligned} \left|I'\right\rangle &= \frac{1}{\sqrt{2^{2n+1}}} \sum_{k=0}^{2^{2n}-1} \left(\cos\theta_k^h|00\rangle + \sin\theta_k^h|10\rangle + \cos\theta_k^s|01\rangle + \sin\theta_k^s|11\rangle\right) \otimes |A_k\rangle \\ &\otimes \left(e^{i\alpha I_k} \cdot e^{i\alpha\Delta I}\right)|0\rangle \otimes |k\rangle \\ \left|I'\right\rangle &= \frac{1}{\sqrt{2^{2n+1}}} \sum_{k=0}^{2^{2n}-1} \left(\cos\theta_k^h|00\rangle + \sin\theta_k^h|10\rangle + \cos\theta_k^s|01\rangle + \sin\theta_k^s|11\rangle\right) \otimes |A_k\rangle \otimes \\ &\left(e^{i\alpha(I_k+\Delta I)}\right)|0\rangle \otimes |k\rangle \end{aligned} \tag{86}$$

Similarly, for contrast, we can use a controlled phase shift gate to scale the intensity values appropriately:

$$e^{i\alpha g_{\mathrm{k}}} = e^{i\alpha\left(\frac{I_k - \min(I)}{\max(I)-\min(I)} \cdot (L-1)\right)} \tag{87}$$

This can be applied to the phase shift operation $R_Z(\theta) = \begin{pmatrix} e^{-i\theta/2} & 0 \\ 0 & e^{i\theta/2} \end{pmatrix}$

Thus, we have

$$\left|I'\right\rangle = \sum_{k=0}^{2^{2n}-1} \left(\cos\theta_k^h|00\rangle + \sin\theta_k^h|10\rangle + \cos\theta_k^S|01\rangle + \sin\theta_k^S|11\rangle\right) \otimes |A_k\rangle \otimes e^{i\alpha g_{\mathrm{k}}}|0\rangle \otimes |k\rangle \tag{88}$$

Figure 15 (b) shows the G_{ct} process.

Selective colour transformations (S_{ct})

In S_{ct}, the operation involves modifying specific colours in an image while leaving others unchanged. This operation allows for precise adjustments to the H, S, and I of selected colours, enhancing or altering specific aspects of the image to achieve the desired effect. Applications of this operation include highlighting specific colours, colour correction, and artistic effects.

In classical cases, selecting pixels whose H values fall within the target range $[H_{\min}, H_{\max}]$ can be mathematically expressed as:

$$H_{\min} \leq H \leq H_{\max} \tag{89}$$

To create a mask M, where each element corresponds to a pixel in the image, we define as:

$$M(i,j) = \begin{cases} 1 & \text{if } H_{\min} \leq H(i,j) \leq H_{\max} \\ 0 & \text{otherwise} \end{cases} \tag{90}$$

where (i, j) denotes the pixel position in the image.

Next, we apply the M to the image to isolate the pixels within the target H range:

$$\text{im}_{\text{selected}} = IM \cdot M$$

where *IM* represents the original classical image.

In quantum representation, we use a controlled $R_z(\theta)$ gate to adjust the *H* of the target pixels. The gate is applied conditionally based on whether the *H* qubits fall within the target range. Additionally, we use a controlled $R_y(\phi)$ gate to adjust the *S*, which modifies the *S* values for the selected colours. For *I*, we employ a controlled phase shift gate $R_z(\alpha\Delta I)$, which modifies the phase factors corresponding to the intensity values. Let's define the new parameters for pixel *k* after the S_{ct} operation: - $\theta_k'^h$: The new angle for hue. - $\theta_k'^s$: The new angle for saturation. - I_k' : The new value for intensity.

That means the transformation rules are:

* If $H_{\min} \leq H_k \leq H_{\max}$ (pixel *k* is selected):

- The hue angle θ_k^h is changed to a new angle $\theta_k'^h$. This change is conceptually due to a controlled $R_z(\theta)$ operation, where θ is the desired hue adjustment. Therefore, $\theta_k'^h = f_H\left(\theta_k^h, \theta\right)$.
- The saturation angle θ_k^s is changed to a new angle $\theta_k'^s$. This is due to a controlled $R_y(\phi)$ operation, where ϕ is the desired saturation adjustment, So, $\theta_k'^s = f_S\left(\theta_k^s, \phi\right)$.
- The intensity I_k is changed to a new value I_k'. This is due to a controlled phase shift $R_z(\alpha\Delta I)$, effectively changing the phase $e^{i\alpha I_k}$ to $e^{i\alpha(I_k+\Delta I)}$ or more generally $e^{i\alpha I_k'}$. Therefore, $I_k' = I_k + \Delta I$ (or some other function $f_I\left(I_k, \Delta I\right)$).

* If $H_k < H_{\min}$ or $H_k > H_{\max}$ (pixel *k* is NOT selected):

- $\theta_k'^h = \theta_k^h$ (hue remains unchanged)
- $\theta_k'^s = \theta_k^s$ (saturation remains unchanged)
- $I_k' = I_k$ (intensity remains unchanged)

Then yields the resulting quantum state of S_{ct}:

$$\left|I'\right\rangle = \sum_{k=0}^{2^{2n}-1} \left(\cos\theta_k'^h|00\rangle + \sin\theta_k'^h|10\rangle + \cos\theta_k'^s|01\rangle + \sin\theta_k'^s|11\rangle\right) \otimes |A_k\rangle \otimes e^{i\alpha I_k'}|0\rangle \otimes |k\rangle \tag{91}$$

Here, $\theta_k'^h, \theta_k'^s$, and I_k' represent the transformed *H*, *D*, and *I* values, respectively.

By following these steps, the (S_{ct}) operation in the AFQIRHSI model can be implemented effectively, ensuring precise and targeted modifications to the image. Figure 15 (c) shows the S_{ct} process.

Quantum Image Retrieval Operation (QMIR)

In any model of quantum images, the only way to obtain the original image or information is by applying measurements [44, 45]. Therefore, in the AFQIRHSI model, to obtain the original image from the quantum representation state, entanglement between the *H* and *S*, as well as between the *A* and *I* is used. The process begins by isolating the components encoded in the quantum state. First, we apply a projective measurement *M* on the qubits encoding the θ_k^h of *H*. This will collapse the state to specific values of *H*, retrieving the *H* information for each pixel. Similarly, we apply the same steps for *S* by performing a *M* on the qubits encoding the θ_k^S of *S*. This collapses the state to specific saturation values, retrieving the *S*.

Since we have *k* indices representing different pixel positions, we apply *M* on each *k*. This measurement collapses the quantum state into one of its basis states with specific probabilities *P*. This operation can be described as:

$$\cos\theta_k^h|00\rangle + \sin\theta_k^h|10\rangle \rightarrow \theta_k^h \tag{92}$$

The measurement effectively projects the state onto the basis states, yielding the value of θ_k^h. The probability of collapsing to $|00\rangle$ or $|10\rangle$ is determined by the coefficients $\cos\theta_k^h$ and $\sin\theta_k^h$, respectively. The superposition $\cos\theta_k^h|00\rangle + \sin\theta_k^h|10\rangle$ represents a quantum state where θ_k^h is encoded as a combination of two basis states, with $\cos\theta_k^h$ and $\sin\theta_k^h$ determining the *P* of the system collapsing into either the $|00\rangle$ or $|10\rangle$. This means *M* in the computational basis collapses the state into either $|00\rangle$ or $|10\rangle$. The *P* of collapsing into $|00\rangle$ is $\left|\cos\theta_k^h\right|^2$, and the *P* of collapsing into $|10\rangle$ is $\left|\sin\theta_k^h\right|^2$.

Similarly, we apply the same steps to θ_k^S. After encoding the saturation information into the quantum state, a *M* is applied, which collapses the quantum state into one of its basis states with specific *P*. This operation can be described as:

$$\cos\theta_k^S|01\rangle + \sin\theta_k^S|11\rangle \rightarrow \theta_k^S \tag{93}$$

The *M* effectively projects the state onto the basis states, yielding the value of θ_k^s. The *P* of collapsing into $|01\rangle$ or $|11\rangle$ is determined by the $\cos\theta_k^s$ and $\sin\theta_k^s$, respectively.

This means the $P(|01\rangle)$ of collapsing into a state $|01\rangle$ is $\left|\cos\theta_k^S\right|^2$, and the $P(|11\rangle)$ of collapsing into a state $|11\rangle$ is $\left|\sin\theta_k^S\right|^2$. Regarding the measurement of $\boldsymbol{A}$ and $\boldsymbol{I}$, it is important to measure the phase of the

qubits encoding the Fourier-transformed intensity $e^{i\alpha I_k}$. This can be done using a quantum phase estimation technique, which retrieves the intensity value I_k from the phase information. Additionally, we apply a M on the qubits encoding the adjacency information $|A_k\rangle$. This measurement retrieves the adjacency information for each pixel, which can be used to understand the pixel's relationship with its neighbours.

To measure the phase of the qubits encoding $e^{i\alpha I_k}$, we use quantum phase estimation techniques $e^{i\alpha I_k}$ that extract I_k from the phase information.

By performing M on $|A_k\rangle$, the classical adjacency information is retrieved as $|A_k\rangle \rightarrow A_k$. The final state on I_k is defined as:

$$\left|I'_k\right\rangle = \left(\theta_k^h|00\rangle + \theta_k^S|01\rangle\right) \otimes |A_k\rangle \otimes I_k|0\rangle \otimes |k\rangle \tag{94}$$

We define the quantum measurement Γ to extract the corresponding information of the pixel (Y, X) :

$$\Gamma = \sum_{YX=0}^{2n-1} I^{\otimes q} \otimes |YX\rangle\langle YX| \tag{95}$$

When applied, this measurement extracts the state:

$$|P_{YX}\rangle = |f(Y,X)\rangle \otimes |YX\rangle \tag{96}$$

In AFQIRHSI, the state becomes:

$$|P_{YX}\rangle = \frac{1}{\sqrt{2^{2n+1}}}\left(\cos\theta_{YX}^h|00\rangle + \sin\theta_{YX}^h|10\rangle + \cos\theta_{YX}^S|01\rangle + \sin\theta_{YX}^S|11\rangle\right) \otimes |A_m\rangle \otimes e^{i\alpha I_k}|0\rangle \otimes |YX\rangle$$

We use the M to recover the H and S values from the quantum state:

$$M = \sum_{m=0}^{2^q=1} m|m\rangle\langle m| \tag{97}$$

We apply M to the state $|f(Y,X)\rangle$, which represents the H and S values:

$$|f(Y,X)\rangle = \cos\theta_{YX}^h|00\rangle + \sin\theta_{YX}^h|10\rangle + \cos\theta_{YX}^s|01\rangle + \sin\theta_{YX}^S|11\rangle \tag{98}$$

Then,

$$\langle f(Y,X)|M|f(Y,X)\rangle \tag{99}$$

$$\begin{aligned} &= \left\langle \cos\theta_{YX}^h \mid 00\right\rangle + \sin\theta_{YX}^h|10\rangle + \cos\theta_{YX}^s|01\rangle \\ &+ \sin\theta_{YX}^s|11\rangle \left| \left(\sum_{m=0}^{2^q-1} m|m\rangle\langle m|\right) \right| \cos\theta_{YX}^h|00\rangle + \sin\theta_{YX}^h|10\rangle + \cos\theta_{YX}^s|01\rangle \\ &+ \sin\theta_{YX}^s|11\rangle \mid \end{aligned} \tag{100}$$

$$\begin{aligned} \langle f(Y,X)|M|f(Y,X)\rangle = \sum_{m=0}^{2^q-1} m \Big(&\left|\cos\theta_{YX}^h\right|^2 \langle 00 \mid m\rangle\langle m \mid 00\rangle + \left|\sin\theta_{YX}^h\right|^2 \langle 10 \mid m\rangle\langle m \mid 10\rangle + \\ &\left|\cos\theta_{YX}^s\right|^2 \langle 01 \mid m\rangle\langle m \mid 01\rangle + \left|\sin\theta_{YX}^s\right|^2 \langle 11 \mid m\rangle\langle m \mid 11\rangle\Big) \end{aligned} \tag{101}$$

For the basis states, let $m = 0$ for $|00\rangle$, $m = 2$ for $|10\rangle$, $m = 1$ for $|01\rangle$ and $m = 3$ for $|11\rangle$ Then,

$$\langle f(Y,X)|M|f(Y,X)\rangle = 0 \cdot \left|\cos\theta_{YX}^h\right|^2 + 2 \cdot \left|\sin\theta_{YX}^h\right|^2 + 1 \cdot \left|\cos\theta_{YX}^s\right|^2 + 3 \cdot \left|\sin\theta_{YX}^s\right|^2$$

Therefore, the P to recover θ_{YX}^S and θ_{YX}^S can be derived using the normalisation conditions for H and S, which state that:

$$\left|\cos\theta_{YX}^S\right|^2 + \left|\sin\theta_{YX}^S\right|^2 = 1, \left|\cos\theta_{YX}^S\right|^2 + \left|\sin\theta_{YX}^S\right|^2 = 1$$

We then obtain the following expression for the pixel value at (Y, X) :

$$f(Y,X) = 2\sin^2\theta_{YX}^h + \cos^2\theta_{YX}^S + 3\sin^2\theta_{YX}^S \tag{102}$$

By applying these steps, the original image can be reconstructed from the measured quantum state. Figure 16 illustrates quantum measurement-based image retrieval in AFQIRHSI.

Quantum Edge Detection Operation (QED)

Quantum edge detection (QED) is a critical operation in QIP that helps identify boundaries within an image. In the AFQIRHSI model, edge detection can be achieved using the adjacency information encoded in $|A_k\rangle$, which captures the relationship between pixels. This information highlights differences in intensity and colour between neighbouring pixels, effectively identifying edges. In our method, we leverage this feature of AFQIRHSI that uses adjacency information for edge detection. Specifically, we use this feature to detect edges in images. In our model, the adjacency information is stored across *p* qubits, with two qubits assigned to the pixel locations, and one qubit for *I* values, and four qubits needed to implement the unitary of the Gaussian filter (U_G). Our approach enhances the Canny edge detection (CED) method[52], integrating it with the AFQIRHSI model. The following steps outline the procedure for our enhanced Canny edge detection (ECED).

The first step in our processing is to load and preprocess the image *I* :

$$I = \{I_{ij} \mid 0 \leq i < M, 0 \leq j < N\} \tag{103}$$

where *M* and *N* are the dimensions of the image. In this step, we represent the intensity values $|I\rangle$ using one qubit, in addition to two qubits for the pixel position *x*, *y*, denoted as $|YX\rangle$. We then apply the operation $R_z(\theta_k)|0\rangle \rightarrow e^{i\alpha I_k}|0\rangle = |I_k\rangle$. Next, we apply quantum smoothing based on the unitary Gaussian filter (U_G), where the Gaussian filter (*GF*) is defined as follows:

$$I' = GF(I, \sigma) \tag{104}$$

To construct the unitary operation U_G in quantum gates for applying the (U_G), we define:

$$U_G = \frac{1}{\sqrt{2\pi\sigma^2}} \sum_x e^{-\frac{x^2}{2\sigma^2}} |x\rangle\langle x| \tag{105}$$

where σ is the standard deviation of the Gaussian kernel (GK). To construct the quantum circuit for unitary GF U_G, we follow three steps. The first step involves applying a quantum Fourier transform (QFT), the second applies a Gaussian weight (GW), and the third involves using an inverse quantum Fourier transform (IQFT) to convert from the frequency domain back to the spatial domain. The implementation of the Gaussian filter can be explained in the following steps: **Step 1.** Apply the QFT to the input state $|x\rangle$, defined as:

$$QFT|x\rangle = \frac{1}{\sqrt{N}} \sum_{k=0}^{N-1} e^{2\pi i \frac{xk}{N}} |k\rangle \tag{106}$$

Step 2. Apply GW in the frequency domain. This is done using controlled phase rotation gates for each frequency component *k* :

$$G(k) = e^{-\frac{k^2}{2\sigma^2}} \tag{107}$$

$$CR_\theta = \begin{cases} e^{-i\theta} & \text{if control qubit is } |1\rangle \\ 1 & \text{otherwise} \end{cases} \tag{108}$$

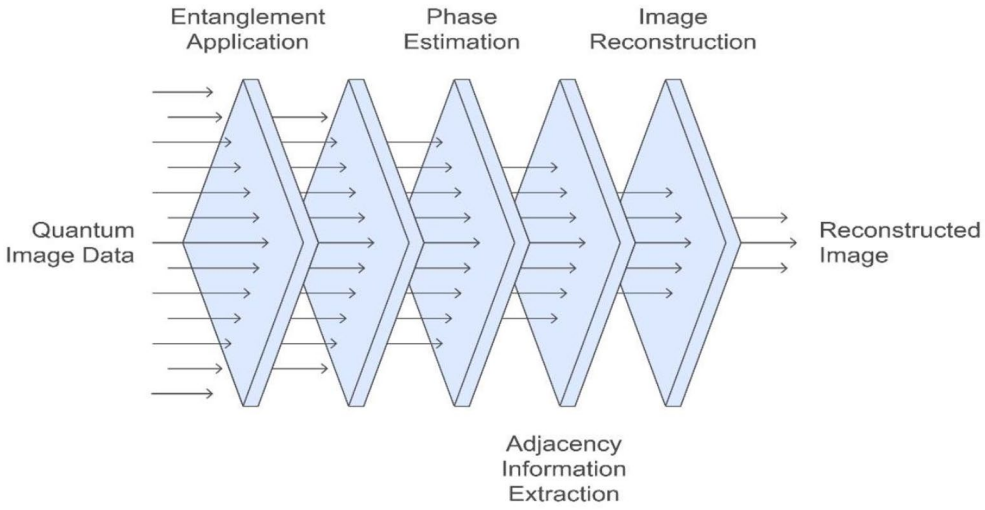

Fig. 16. Quantum measurement-based image retrieval in AFQIRHSI.

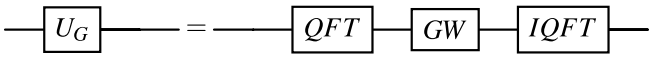

Fig. 17. Quantum circuit of U_G.

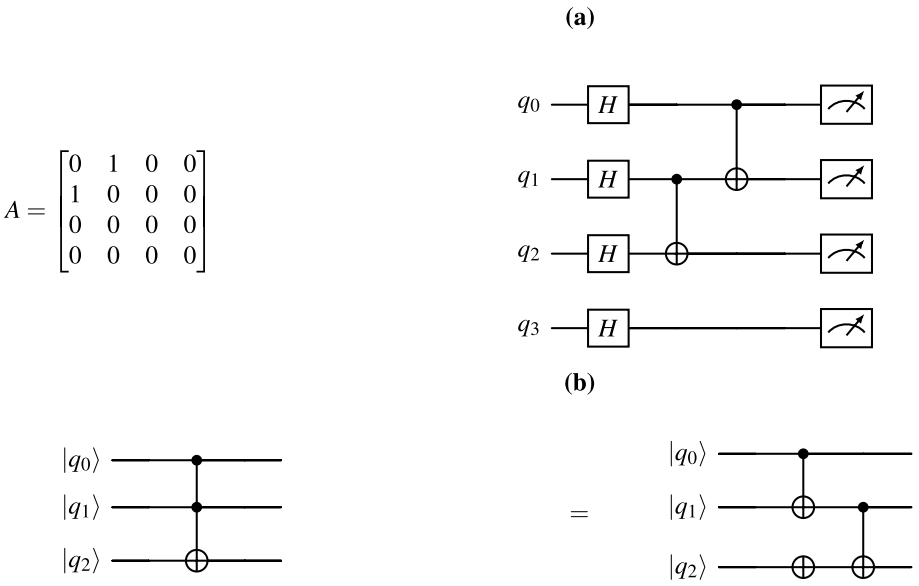

Fig. 18. (**a**) Adjacency matrix and its corresponding quantum circuit, and (**b**) quantum circuit to compute the difference between two qubits.

Where $\theta = \frac{k^2}{2\sigma^2}$. **Step 3.** Apply IQFT:

$$IQFT|k\rangle = \frac{1}{\sqrt{N}} \sum_{x=0}^{N-1} e^{-2\pi i \frac{xk}{N}} |x\rangle \tag{109}$$

The quantum circuit of U_G operation is shown in Fig. 17.

Next, we calculate A_{ij}, defined as:

$$A_{ij} = \left\{ A_{ij}^{\text{up}}, A_{ij}^{\text{down}}, A_{ij}^{\text{left}}, A_{ij}^{\text{right}} \right\}$$

where $A_{ij}^{\text{direction}}$ is defined as follows:

$$A_{ij}^{\text{up}} = \begin{cases} \left| I'_{ij} - I'_{i-1,j} \right| & \text{if } i > 0 \\ 0 & \text{otherwise} \end{cases}$$

$$A_{ij}^{\text{down}} = \begin{cases} \left| I'_{ij} - I'_{i+1,j} \right| & \text{if } i < M-1 \\ 0 & \text{otherwise} \end{cases}$$

$$A_{ij}^{\text{left}} = \begin{cases} \left| I'_{ij} - I'_{i,j-1} \right| & \text{if } j > 0 \\ 0 & \text{otherwise} \end{cases}$$

$$A_{ij}^{\text{right}} = \begin{cases} \left| I'_{ij} - I'_{i,j+1} \right| & \text{if } j < N-1 \\ 0 & \text{otherwise} \end{cases}$$

To construct A_{ij}, a NOT gate or X gate can be used, as shown in Fig. 6 (a), to modify the values. Suppose we have the adjacency information from equation (25). The quantum circuit corresponding to equation (25) is shown in Fig. 18 (a).

In the following steps, we will use the Frobenius norm (also called the Euclidean norm) $\| \Delta A_{kl} \|_F$ of the difference matrix to obtain a scalar value representing the difference. The $\| \Delta A_{kl} \|_F$ can be defined as:

$$\| \Delta A_{kl} \|_F = \sqrt{\sum_{i,j} |A_k(i,j) - A_l(i,j)|^2} \tag{110}$$

The unitary operation $U_{\Delta A}$ computes the difference between the adjacency matrices of neighbouring pixels k and l, defined as:

$$U_{\Delta A} : |A_k\rangle |A_l\rangle |0\rangle \rightarrow |A_k\rangle |A_l\rangle |A_k - A_l\rangle \tag{111}$$

Each matrix requires four qubits, and to compute the difference between two qubits, we need to apply a CNOT gate, with an ancillary qubit to store the result (see Fig. 18 (b)).

Next, we apply the chosen thresholds T_{high} , T_{low} , and $T_{\text{adjacency}} = T_{\text{adj}}$. The edge detection is then defined based on the following condition:

$$Edge_{kl} = \begin{cases} 1 & \text{if } \|\Delta A_{kl}\|_F > T \\ 0 & \text{otherwise} \end{cases}$$

The quantum circuit gates for computing adjacency differences and the Frobenius norm are shown in Fig. 19 (a). The quantum circuit gate for applying thresholds, which compares two values, is shown in Fig. 19 (b).

The final state $|\Psi_{\text{edges}}\rangle$ after edge detection is:

$$|\Psi_{\text{edges}}\rangle = \sum_{k,l} Edge_{kl} \otimes \left| \text{adjacency differences} \right\rangle \tag{112}$$

An example of QED is shown with the original matrix and the smoothed matrix, where the original intensity matrix is:

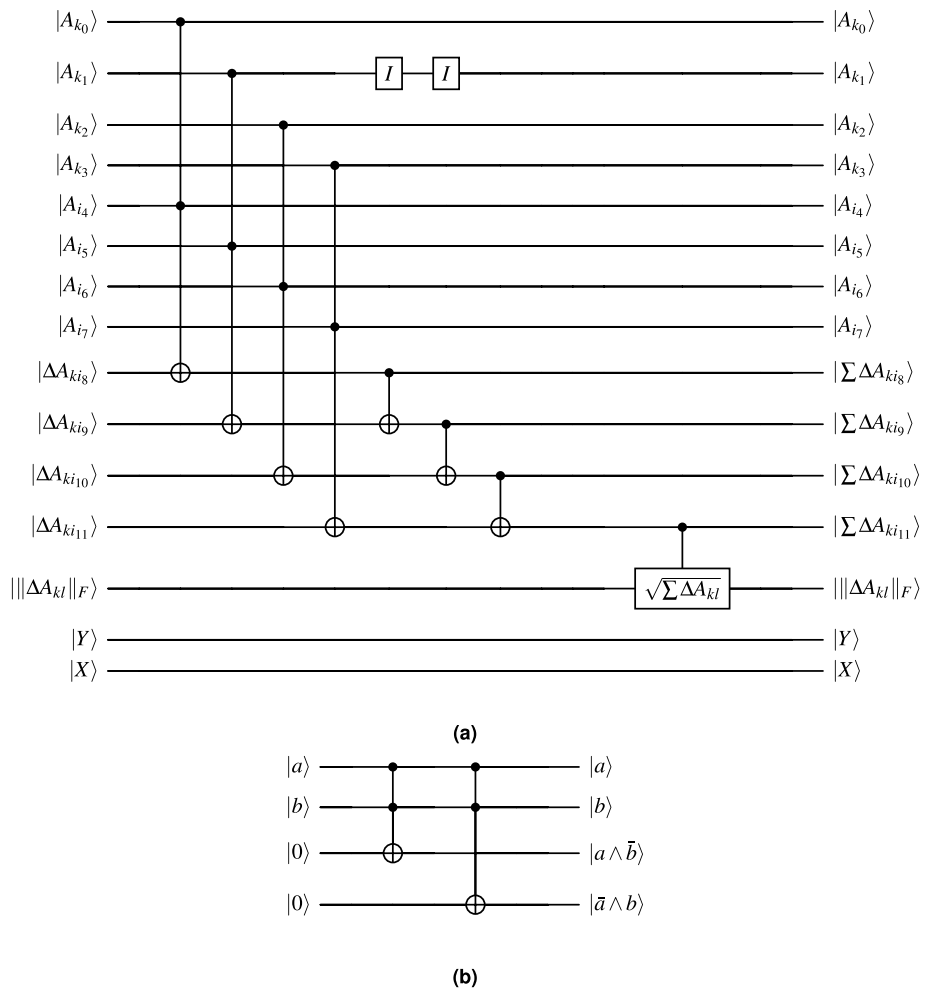

Fig. 19. (**a**) Quantum circuit for computing the difference between A_k and A_l and (**b**) comparison between two values using a quantum circuit.

$$\begin{bmatrix} 148 & 105 & 62 & 121 & \dots & 116 & 119 \\ 159 & 142 & 124 & 118 & \dots & 116 & 116 \\ 185 & 174 & 161 & 118 & \dots & 117 & 116 \\ 171 & 170 & 168 & 5 & \dots & 0 & 0 \\ 170 & 169 & 166 & 10 & \dots & 1 & 0 \\ 169 & 168 & 164 & 16 & \dots & 2 & 0 \end{bmatrix}$$

and smoothed intensity matrix is:

$$\begin{bmatrix} 142 & 120 & 96 & 118 & \dots & 117 & 116 \\ 159 & 142 & 124 & 118 & \dots & 116 & 116 \\ 185 & 174 & 161 & 118 & \dots & 117 & 116 \\ 171 & 170 & 168 & 5 & \dots & 0 & 0 \\ 170 & 169 & 166 & 10 & \dots & 1 & 0 \\ 169 & 168 & 164 & 16 & \dots & 2 & 0 \end{bmatrix}$$

The result, shown in Fig. 20, presents thresholds set as high as 50, as low as 20, and adjusted thresholds of 10.

Figure 21 shows the results of our simulation after applying the proposed QED, compared with the Canny edge detection method.

Quantitative advantage of AFQIRHSI

This section introduces the quantitative advantage of the AFQIRHSI model and the compression performance to QIRHSI and EQIRHSI models. The AFQIRHSI model demonstrates a clear more advantage comparison with its predecessors either QIRHSI or EQIRHSI in terms of qubit economy (number of qubits), circuit depth (number of gates), and information density (measure of how much image information such as pixel values, colors, positions). Via incorporating two innovations features, the first on is Fourier-encoded intensity, instead of using binary qubits and adjacency-based entanglement to cover the relationship between neighbourhood pixels, AFQIRHSI reduces the total number of qubits required by a constant three qubits across all image

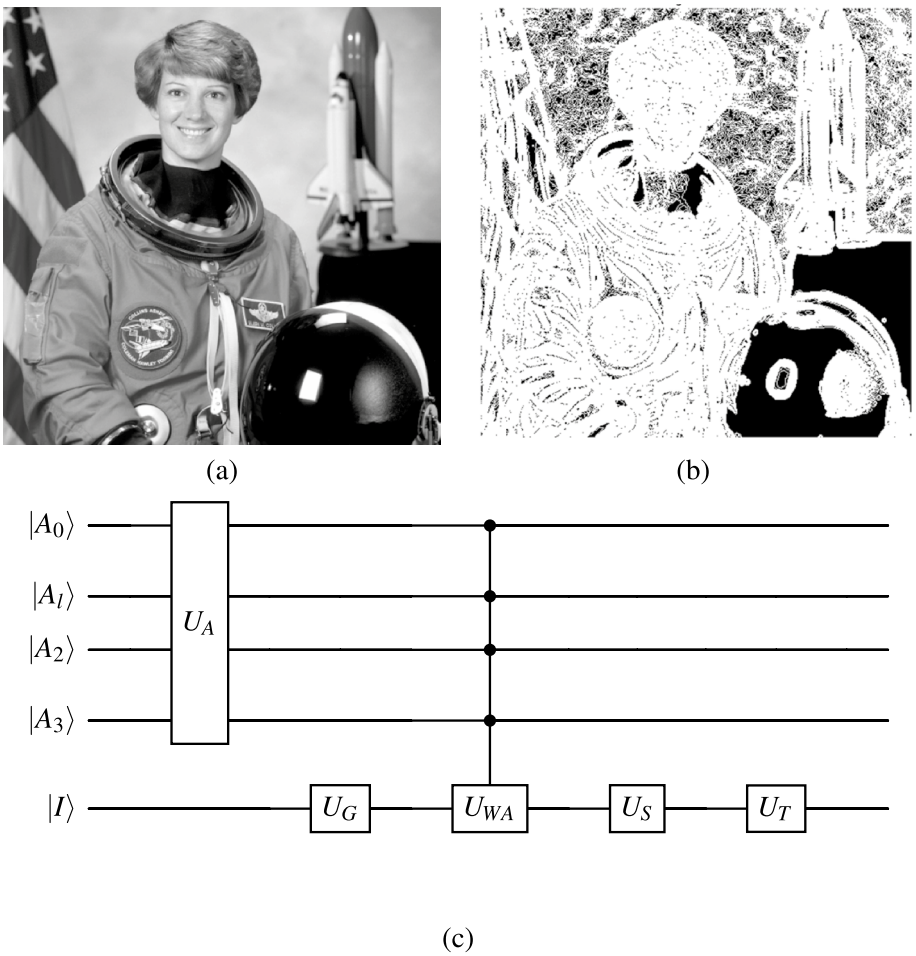

Fig. 20. (**a**) Original image[53], (**b**) image after applying the QED based on AFQIRHSI, and (**c**) quantum circuit of QED based on AFQIRHSI.

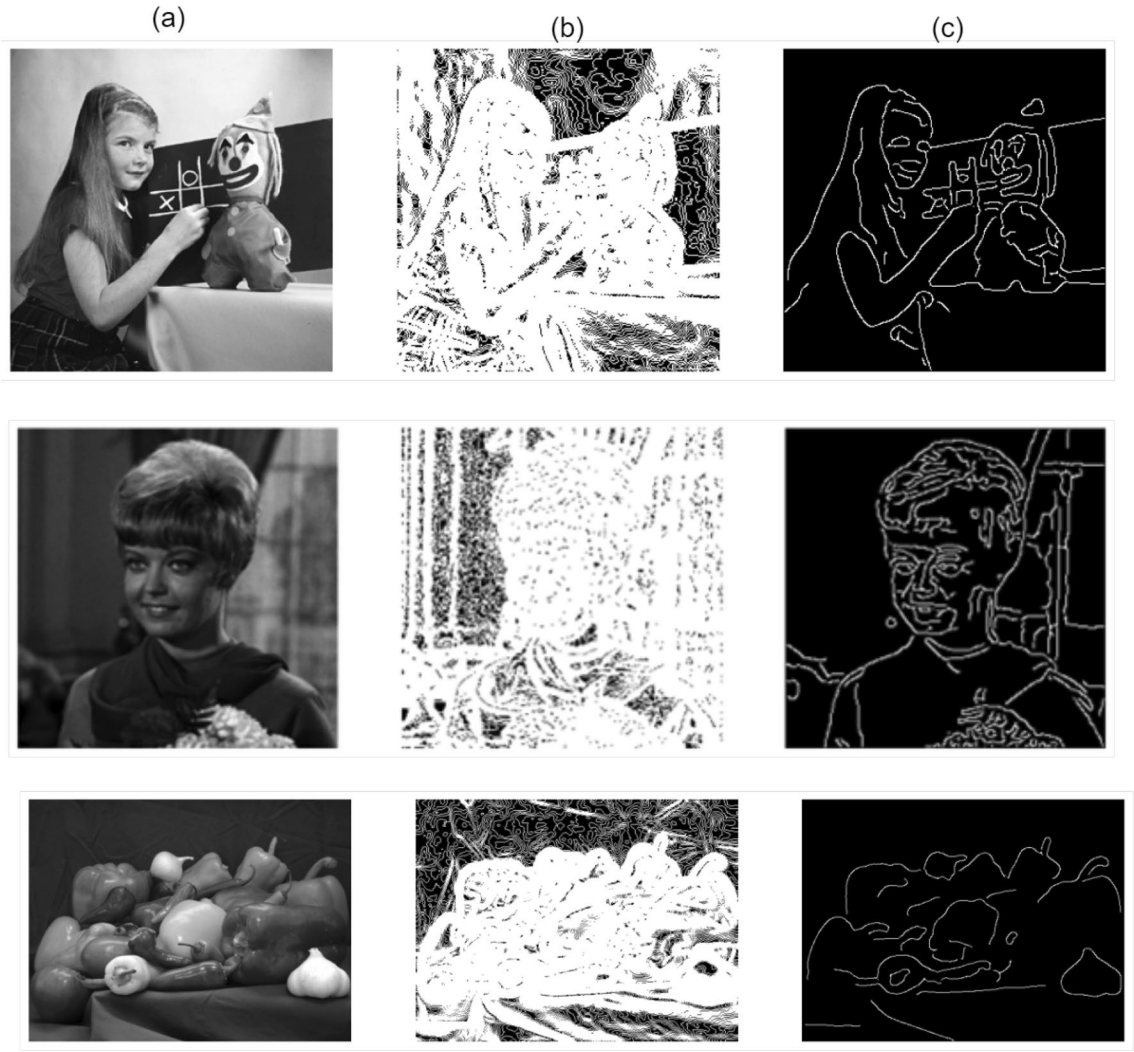

Fig. 21. (**a**) Original image, (**b**) image after applying QED of AFQIRHSI, and (**c**) Canny edge detection method.

sizes, translating to an 11 19 qubit saving in practical ranges ($n = 3 - 10$). Additionally, it achieves the same preparation depth as QIRHSI and halves that of EQIRHSI, while maintaining a competitive gate count. Notably, by storing intensity information in the Fourier basis, AFQIRHSI allows selective gate application to significant spectral coefficients, improving scalability to large images and, simultaneously, in cryptography. The adjacency matrix $|A_k\rangle$, entangled with the Fourier-phase intensity, provides native support for edge and texture semantics without additional post-processing. Quantitative analysis reveals that AFQIRHSI achieves the highest storage density (pixels per qubit) among all compared models, while simultaneously embedding spatial context into the quantum state. These improvements position AFQIRHSI as a more resource-efficient and semantically rich model, particularly suitable for near-term quantum image processing tasks involving cryptography, edge detection, and structural analysis.

Our model inherits the H and S entanglement of EQIRHSI and folds two further optimizations into the preparation circuit, first one: Fourier-encoded intensity, by storing I_k in the Fourier basis, only the significant spectral coefficients need controlled rotations; low-energy coefficients are skipped, therefore, and based on analysis of this state the intensity register is prepared with $\mathcal{O}(q \log q)$ rather than $\mathcal{O}(q2^{2n})$ gates. Table 4 shows the resource-and-compression for several sizes of image where $n = 3 \ldots 10$, and common parameters; colour-bit-depth $q = 8$; adjacency register $p = 4$. Therefore, based on this feature, we have the question why AFQIRHSI keeps the edge? To answer this question. We must drive deeply on each model; begin with number of qubits; all n values show the same saving: $Q_{\mathrm{AFQIRHSI}} = 2n + 7 < Q_{\mathrm{QIRHSI/EQIRHSI}} = 2n + 10$, where Q is number of qubits. That is a constant three-qubit advantage ($\approx 11\%$ when $n \geq 6$), where AFQIRHSI needs 13 qubits for an 8×8 image versus 16 for QIRHSI/EQIRHSI (-19%). This resource efficiency extends to execution time, as AFQIRHSI's preparation depth is the same as the baseline QIRHSI (scaling as $4 \cdot 2^4 n$) and half that of EQIRHSI. The trade-off for this superior qubit and depth performance is a higher gate count; the AFQIRHSI gatecount, with a leading term of $8 \cdot 2^4 n$, is on par with the more complex EQIRHSI model. This highlights the model's key advantage of making a favorable trade to achieve its goals. AFQIRHSI has a new advantage feature which

n	Model	Qubits	Depth (≈)	Gates (≈)	Pixels/Qubit *	Edge-information
3	QIRHSI	16	1.64×10^4	1.79×10^4	4.00	—
	EQIRHSI	16	3.28×10^4	3.43×10^4	4.00	—
	AFQIRHSI	13	1.64×10^4	3.32×10^4	4.92	✓
4	QIRHSI	18	2.62×10^5	2.70×10^5	14.22	—
	EQIRHSI	18	5.24×10^5	5.32×10^5	14.22	—
	AFQIRHSI	15	2.62×10^5	5.27×10^5	17.07	✓
5	QIRHSI	20	4.19×10^6	4.24×10^6	51.20	—
	EQIRHSI	20	8.39×10^6	8.43×10^6	51.20	—
	AFQIRHSI	17	4.19×10^6	8.40×10^6	60.24	✓
6	QIRHSI	22	6.71×10^7	6.73×10^7	186.18	—
	EQIRHSI	22	1.34×10^8	1.34×10^8	186.18	—
	AFQIRHSI	19	6.71×10^7	1.34×10^8	215.58	✓
7	QIRHSI	24	1.07×10^9	1.07×10^9	682.67	—
	EQIRHSI	24	2.15×10^9	2.15×10^9	682.67	—
	AFQIRHSI	21	1.07×10^9	2.15×10^9	780.19	✓
8	QIRHSI	26	1.72×10^{10}	1.72×10^{10}	2520.62	—
	EQIRHSI	26	3.44×10^{10}	3.44×10^{10}	2520.62	—
	AFQIRHSI	23	1.72×10^{10}	3.44×10^{10}	2849.39	✓
9	QIRHSI	28	2.75×10^{11}	2.75×10^{11}	9362.29	—
	EQIRHSI	28	5.50×10^{11}	5.50×10^{11}	9362.29	—
	AFQIRHSI	25	2.75×10^{11}	5.50×10^{11}	10485.76	✓
10	QIRHSI	30	4.40×10^{12}	4.40×10^{12}	34952.53	—
	EQIRHSI	30	8.80×10^{12}	8.80×10^{12}	34952.53	—
	AFQIRHSI	27	4.40×10^{12}	8.80×10^{12}	38836.15	✓

Table 4. Resource comparison for QIRHSI, EQIRHSI, and AFQIRHSI models across various image sizes.

Model	Qubits	Circuit depth ≈	Gates ≈	*Pixels/qubit*	Edge-information	Quantum cost
QIRHSI	16	$2^{4n+2} = 1.6 \times 10^4$	16,774	4.00	—	baseline
EQIRHSI	16	$8 \cdot 2^{4n} = 3.3 \times 10^4$	32,647	4.00	—	+94% vs QIRHSI
AFQIRHSI	13	$4 \cdot 2^{4n} = 1.6 \times 10^4$	33,226	4.92	built-in	+98% vs QIRHSI

Table 5. Resource/compression comparison for an 8×8 image ($n = 3, q = 8, p = 4$).

is the four-qubit adjacency register is entangled with the Fourier-phase intensity, giving built-in edge, texture semantics that the other models lack. In every image size studied Table 5, show the AFQIRHSI the highest storage density, the same of QIRHSI or shallower of EQIRHSI circuit depth, and only model is including edge information. A four qubit register $|A_k\rangle$ (left, right, up, down) is entangled with the intensity phase. This supplies pixel-to-pixel context "for free" at retrieval time, enabling quantum edge or texture operators without an external neighborhood pass. These quantitative facts substantiate AFQIRHSI's claimed advantage. Table 5 shows the number of qubits, circuit depth, edge information and quantum cost. Because of these two ingredients features of AFQIRHSI are using fewer qubits than its predecessors, reaches the same (or lower) circuit depth, yet provides spatial semantics that QIRHSI or EQIRHSI lack. Moreover, the quantum cost for these three models reveals that AFQIRHSI requires more resources than the other models due to the extensive amount of information it processes (see Table 6). Figures 22, 23, 24 and 25 shows original image of king Ashurbanipal, and the quantum circuit for QIRHSI, EQIRHSI and AFQIRHSI of original image where $n = 2$ that is mean ($2 \times 2 = 4 \times 4$), respectively. Also, Fig. 26 shows the quantum measurement histogram (qmh) comparison of three models of HSI color model based QIR methods. (a) QIRHSI employs independent hue and saturation encoding with binary intensity representation, utilizing 12 qubits and demonstrating uniform state distribution across 340 unique measurement outcomes. while (b) refer to the qmh of EQIRHSI which achieving improved measurement efficiency with structured state patterns. whereas (c) AFQIRHSI providing the most comprehensive spatial-color correlation analysis through 9 qubits with advanced edge detection capabilities. All measurements performed

Model	Quantum cost expression	Quantum cost for $n = 3$
QIRHSI	$2^{4n+2} + qn \times 2^{2n} + 2n - 3 \times 2^{2n+1}$	16,774
EQIRHSI	$8 \cdot 2^{4n} - 3 \cdot 2^{2n+1} + qn \cdot 2^{2n} + 2n + 1$	32,647
AFQIRHSI	$8 \cdot 2^{4n} + (pn - 5) \cdot 2^{2n} + 2n + p$	33,226

Table 6. Comparison of quantum costs across three models: QIRHSI, EQIRHSI, and AFQIRHSI.

Fig. 22. Original image of King Ashurbanipal[54].

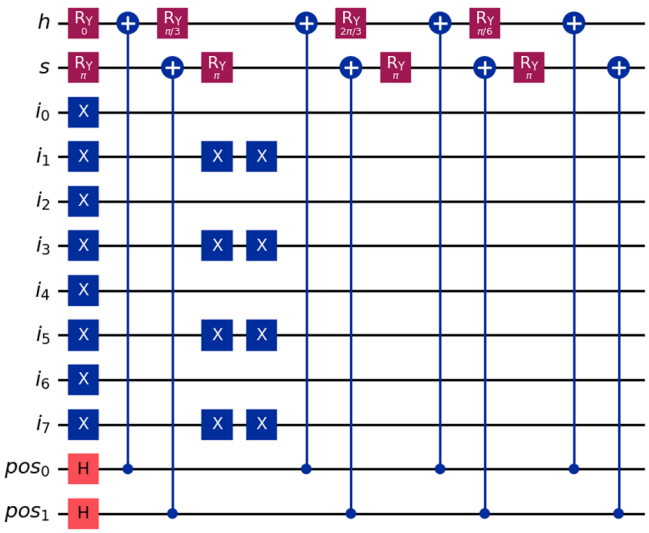

Fig. 23. Quantum image representations of QIRHSI of Fig. 22 where $n = 2$.

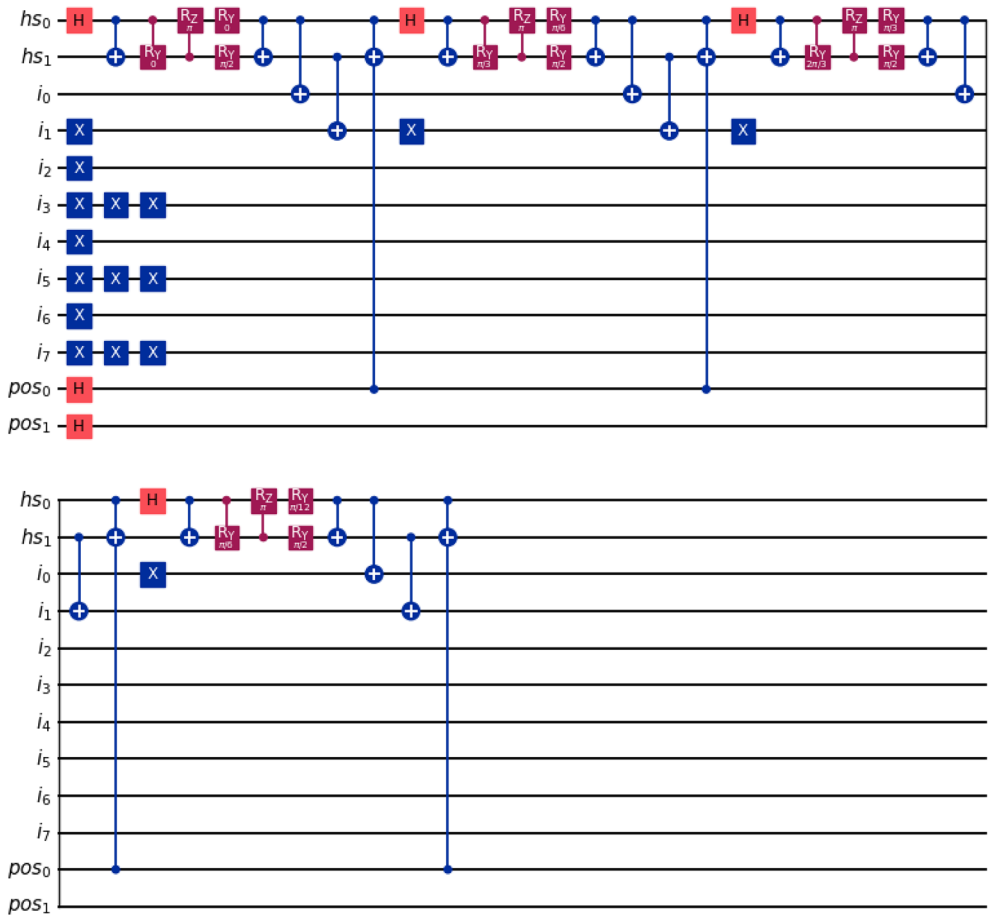

Fig. 24. Quantum image representation of EQIRHSI of Fig. 22 where $n = 2$.

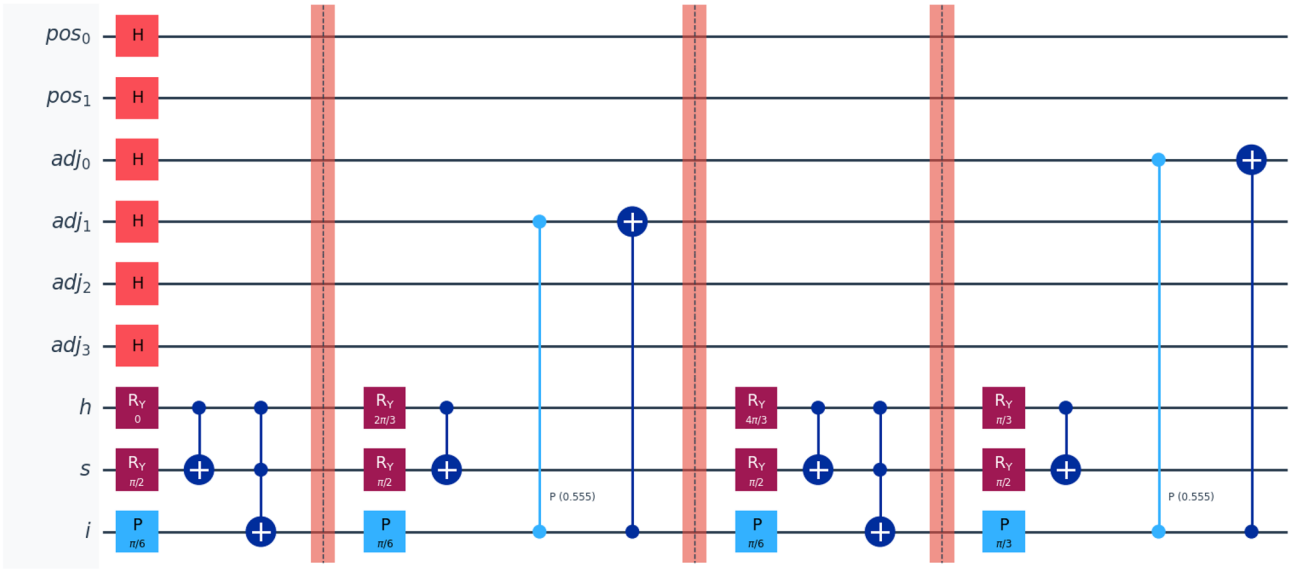

Fig. 25. Quantum image representations of AFQIRHSI of Fig. 22 where $n = 2$.

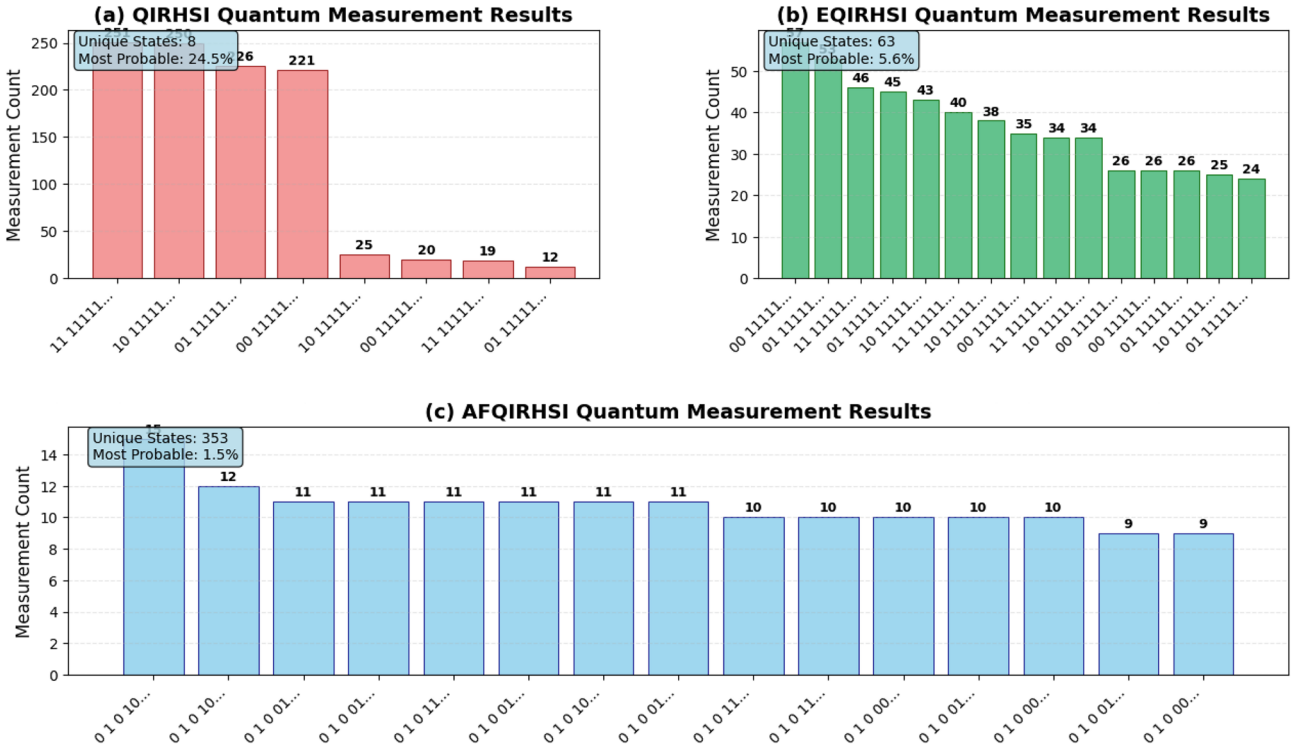

Fig. 26. Quantum measurement histogram comparison of (**a**) QIRHSI, (**b**) EQIRHSI and (**c**) AFQIRHSI of Figs. 23, 24 and 25, respectively.

with 1,024 shots demonstrate the distinct quantum state distributions characteristic of each encoding approach, highlighting the evolution from independent encoding (QIRHSI) to single entanglement (EQIRHSI) to dual entanglement with spatial information (AFQIRHSI).

(a) QIRHSI Quantum Measurement Results

* Unique States (8): The histogram is dominated by a few very probable outcomes.
* Probability (24.5%): The most probable state is quite common.
* Interpretation: This model uses independent qubits for H and S, which are treated separately. It does not capture complex relations; it only encodes simple, universal features. The absence of entanglement between colors gives a more tractable final state, so the histogram is more "spiky." It's akin to snapping a very blurry, low-resolution photo of the image's features.

(b) EQIRHSI Quantum Measurement Results

* Unique States (63): The number of unique outcomes is significantly higher.
* Lower Probability (5.6%): The probabilities are more spread out; no single state is overwhelmingly dominant.
* Interpretation: This entanglement produces a more complicated superposition describing the correlation between H and S: the circuit can now encode richer (color) information, allowing for a larger set of possible measurement outcomes with a more uniform histogram.

(c) AFQIRHSI Quantum Measurement Results

* Unique States (353): A huge number of unique outcomes were measured.
* Very Low Probability (1.5%): The histogram is very flat, that is mean the probability of any single state is very low.
* Interpretation: This is the most advanced model. It uses dual entanglement (H-S and A_k Adjacency-Intensity) and a Fourier transform for intensity, creating an incredibly complex and rich quantum state.
    * The flat histogram is a sign of its expressive power. This means the circuit has successfully encoded vast interconnected information (color, position, and local texture via adjacency) into superposition.
    * The final state is spread across many possibilities. It captures a few dominant features, but a broad spectrum of subtleties and correlations. A high count for a particular state here would indicate a powerful and complex feature that includes color, texture, and location within these 2×2 image.

where **Pixels/Qubit** * is a ratio that measures the storage density or efficiency of each quantum image model, and we can express it using the mathematical equation: `Pixels/Qubit = (Total Number of Pixels)/(Total Number of Qubits)`.

Conclusion, discussion and future directions

Quantum image processing merges quantum mechanics with image processing, aiming to provide innovative methods for handling complex visual data. While conventional computing struggles with the increasing complexity of image tasks, quantum computing benefits from quantum properties such as entanglement and superposition, enabling information to be processed in novel and time-efficient ways. In this context, a new QIR model based on the HSI colour space, called adjacency Fourier quantum image representation of HSI (AFQIRHSI), is introduced in the present work. In AFQIRHSI, two principles of quantum mechanics - quantum superposition and entanglement - are utilised to offer a comprehensive and efficient approach to QIR. The construction of AFQIRHSI involves entanglement structures of the Fourier transform for intensity values, an adjacency matrix of pixels for spatial relationships, and dual entanglement structures for H and S. AFQIRHSI significantly enhances the capabilities and precision of QIR. The AFQIRHSI model utilises $2n + p + 3$ qubits to represent a colour digital image of size $(2^n \times 2^n)$, where $p = 4$ in our model for the adjacency matrix. AFQIRHSI not only improves storage capacity by factors of 4 and 2 compared to previous models, such as QIRHSI and EQIRHSI, respectively, but also enhances efficiency in image encoding and retrieval. Furthermore, a comparative analysis presented herein demonstrates that AFQIRHSI outperforms existing QIRHSI and EQIRHSI models in terms of flexibility, efficiency, and the capability to handle complex image data. Additionally, several operations using quantum circuits - such as the complement colour transformation U_{CC}, global colour transformation U_{st}, selective colour transformations S_{ct}, quantum image retrieval *QMIR*, and quantum image detection operations *QED* - are provided.

AFQIRHSI offers many significant advantages, primarily in its superior qubit efficiency. It represents a $2^n \times 2^n$ color image using $2n + 7$ qubits, which constitutes a constant 3-qubit saving over QIRHSI and EQIRHSI (e.g., approximately 19% reduction for an 8×8 image; see Table 4). This leads to the highest storage density (pixels per qubit) among the compared models (e.g., 4.92 vs. 4.00 at $n = 3$), making AFQIRHSI more effective for quantum image representation. Additionally, AFQIRHSI improves near-term feasibility by achieving an optimized preparation circuit depth, which is less than half that of EQIRHSI and comparable to QIRHSI ($O(4 \cdot 2^{4n})$). Notably, its entanglement of an adjacency matrix with four neighboring pixels (up, down, left, right) and Fourier-phase intensity provides native support for edge and texture semantics without requiring additional post-processing, a feature absent in its predecessors. This makes AFQIRHSI uniquely capable among existing models. Furthermore, the dual entanglement for hue (H) and saturation (S) ensures accurate color depiction, while Fourier-encoded intensity enables compact representation and scalability through selective gate application. Some advantages of the AFQIRHSI model include enhanced colour representation, where the entanglement between the hue (H) and saturation (S) components ensures a more natural and accurate depiction of colours. The entanglement between the Fourier transform and adjacency matrix provides a powerful method for encoding spatial relationships, which is essential for edge detection and intricate image manipulations. In addition, AFQIRHSI requires fewer operations for comprehensive image transformations compared to the QIRHSI and EQIRHSI models. Moreover, the model is particularly effective for applications like edge detection, where detailed image analysis and secure encryption are critical. Despite the complex mathematical formulas, the AFQIRHSI model outperforms other models, such as QIRHSI and EQIRHSI, by providing superior performance and enhanced capabilities. Its dual structure, offering both superposition and entanglement, and the integration of adjacency information represented by the adjacency matrix, make it a robust and versatile tool for quantum image processing. This paves the way for more advanced and efficient applications of quantum computing. Regarding future directions, the new model AFQIRHSI can be applied in several fields such as quantum cryptography, quantum image processing (QIP), and Artificial Intelligence (AI). Its strength lies in using both AFQIRHSI features, adjacency information (A_k), and Fourier-transformed intensity (I_k) to represent images, opening up novel applications. In quantum cryptography, AFQIRHSI could enhance quantum key distribution (QKD) by securely embedding keys into quantum images, be used for developing robust encryption algorithms based on theta of H and S, and *phi* of I, and using adjacency matrices for spatial encoding, and enable quantum steganography for covert information embedding. Additionally, integrating AFQIRHSI with quantum chaotic systems could generate complex cryptographic keys for dynamic encryption protocols. Furthermore, these features could enable using AFQIRHSI in quantum image processing. Its benefits can be seen in quantum image segmentation, where using adjacency and intensity features could lead to algorithms that more efficiently and accurately cluster pixels into meaningful regions compared to other methods. This directly applies to medical image analysis (e.g., quantifying tissue connectivity changes in neurodegenerative diseases from MRI/DTI scans) and object recognition through enhanced feature representation. Also, in the future, AFQIRHSI could be used in AI, specifically in Quantum Machine Learning (QML), for feature extraction from images such as edge detection, face detection, and other applications. This idea allows adjacency patterns and specific Fourier intensity coefficients to be transformed into robust feature vectors. This would enhance the performance of QML classifiers for tasks like texture analysis or anomaly detection. Similarly, integrating AFQIRHSI-derived features with AI for advanced image classification and using them in quantum or hybrid quantum-classical Convolutional Neural Networks (CNNs) is a promising research path.

Data availability

All data analysed during this study are included in this published article and could be accessed directly via [references[47,48,53] and[54] of the list of references].

Received: 6 January 2025; Accepted: 10 October 2025
Published online: 17 November 2025

References

1. Sungheetha, D. A. Applications and Challenges of Quantum Image Processing–A Comprehensive review, *rrrj,* **2**(1), 112-121 (2023).
2. Arute, F. et al. Quantum supremacy using a programmable superconducting processor. *Nature* **574**(7779), 505–510 (2019).
3. Su, J., Guo, X., Liu, C. & Li, L. A new trend of quantum image representations. *IEEE Access* **8**, 214520–214537 (2020).
4. Feynman, R. P., Simulating physics with computers, in *Feynman and computation.* 133-153 (CRC Press, 2018).
5. Shor, P. W., Algorithms for quantum computation: discrete logarithms and factoring, in *Proceedings 35th annual symposium on foundations of computer science* 124-134 (IEEE, 1994).
6. Grover, L. K., A fast quantum mechanical algorithm for database search, in *Proceedings of the twenty-eighth annual ACM symposium on Theory of computing* 212-219 (1996).
7. Nielsen, M. A., & Chuang, I. L., Quantum computation and quantum information. (Cambridge University Press, 2010).
8. Le, P. Q., Dong, F. & Hirota, K. A flexible representation of quantum images for polynomial preparation, image compression, and processing operations. *Quantum Information Processing* **10**, 63–84 (2011).
9. Gonzalez, R. C., Woods, R. E.& Eddins, S. L. *Digital Image Processing*, 262 (Publishing House of Electronics Industry, Beijing, China, 2002).
10. Fu, X., Ding, M., Sun, Y., & Chen, S., A new quantum edge detection algorithm for medical images, in *MIPPR 2009: Medical Imaging, Parallel Processing of Images, and Optimization Techniques* **7497,** 547-553 (SPIE, 2009).
11. Li, H.-S., Fan, P., Xia, H.-Y., Peng, H. & Song, S. Quantum implementation circuits of quantum signal representation and type conversion. *IEEE Transactions on Circuits and Systems I: Regular Papers* **66**(1), 341–354 (2018).
12. Benioff, P. The computer as a physical system: A microscopic quantum mechanical Hamiltonian model of computers as represented by Turing machines. *Journal of Statistical Physics* **22**, 563–591 (1980).
13. Caraiman, S. & Manta, V. I. Image segmentation on a quantum computer. *Quantum Information Processing* **14**, 1693–1715 (2015).
14. Nielsen M. A. & Chuang, I. (ed.) *Quantum computation and quantum information.* (American Association of Physics Teachers, 2002).
15. Venegas-Andraca, S. E. & Bose, S. Quantum computation and image processing: New trends in artificial intelligence, *in IJCAI*, **1563 (**2003**).**
16. Yan F. & Venegas-Andraca, S. E. Quantum image processing. (Springer Nature, 2020).
17. Iliyasu, A. M., Le, P. Q., Dong, F. & Hirota, K. Watermarking and authentication of quantum images based on restricted geometric transformations. *Information Sciences* **186**(1), 126–149 (2012).
18. Song, X.-H., Wang, S., Liu, S., Abd El-Latif, A. A., & Niu, X.-M. A dynamic watermarking scheme for quantum images using quantum wavelet transform, *Quantum Information Processing*, **12,** 3689-3706 (2013).
19. Abd-El-Atty, B., A. Abd El-Latif, A., & Amin, M., New quantum image steganography scheme with Hadamard transformation, in *Proceedings of the International Conference on Advanced Intelligent Systems and Informatics 2016*, 342-352 (Springer, 2017).
20. Jiang, N., Zhao, N. & Wang, L. LSB based quantum image steganography algorithm. *International Journal of Theoretical Physics* **55**(1), 107–123 (2016).
21. Song, X. H., Wang, H. Q., Venegas-Andraca, S. E., & Abd El-Latif, A. A., Quantum video encryption based on qubit-planes controlled-XOR operations and improved logistic map, *Physica A: Statistical Mechanics and its Applications*, **537**, 122660 (2020).
22. He, J., Zhu, H. & Zhou, X. Quantum image encryption algorithm via optimized quantum circuit and parity bit-plane permutation. *Journal of Information Security and Applications* **81**, 103698 (2024).
23. Luo, Y., Tang, S., Liu, J., Cao, L. & Qiu, S. Image encryption scheme by combining the hyper-chaotic system with quantum coding. *Optics and Lasers in Engineering* **124**, 105836 (2020).
24. Venegas-Andraca, S. E. & Bose, S., Storing, processing, and retrieving an image using quantum mechanics, in *Quantum Information and Computation*, **5105**, 137-147 (SPIE, 2003).
25. Venegas-Andraca, S. E. & Ball, J. Processing images in entangled quantum systems. *Quantum Information Processing* **9**(1), 1–11 (2010).
26. Latorre, J. I. Image compression and entanglement, arXiv preprint quant-ph/0510031, (2005).
27. Sun, B. et al., A multi-channel representation for images on quantum computers using the RGBα color space, in *2011 IEEE 7th International Symposium on Intelligent Signal Processing*, 1-6 (IEEE, 2011).
28. Li, H.-S., Zhu, Q., Zhou, R.-G., Song, L. & Yang, X.-J. Multi-dimensional color image storage and retrieval for a normal arbitrary quantum superposition state. *Quantum Information Processing* **13**, 991–1011 (2014).
29. Li, H.-S., Chen, X., Xia, H., Liang, Y. & Zhou, Z. A quantum image representation based on bitplanes. *IEEE Access* **6**, 62396–62404 (2018).
30. Zhang, Y., Lu, K., Gao, Y. & Wang, M. NEQR: a novel enhanced quantum representation of digital images. *Quantum Information Processing* **12**, 2833–2860 (2013).
31. Sun, B., Iliyasu, A., Yan, F., Dong, F. & Hirota, K. An RGB multi-channel representation for images on quantum computers, *J. Adv. Comput. Intell. Intell. Inform*, **17**(3) (2013).
32. Sang, J., Wang, S. & Li, Q. A novel quantum representation of color digital images. *Quantum Information Processing* **16**, 1–14 (2017).
33. Jiang, N., Wang, J. & Mu, Y. Quantum image scaling up based on nearest-neighbor interpolation with integer scaling ratio. *Quantum Information Processing* **14**(11), 4001–4026 (2015).
34. Abdolmaleky, M., Naseri, M., Batle, J., Farouk, A. & Gong, L.-H. Red-Green-Blue multi-channel quantum representation of digital images. *Optik* **128**, 121–132 (2017).
35. Şahin, E. & Yilmaz, I. QRMW: quantum representation of multi wavelength images. *Turkish Journal of Electrical Engineering and Computer Sciences* **26**(2), 768–779 (2018).
36. Wang, L., Ran, Q., Ma, J., Yu, S. & Tan, L. QRCI: A new quantum representation model of color digital images. *Optics Communications* **438**, 147–158 (2019).
37. Wang, L., Ran, Q. & Ma, J. Double quantum color images encryption scheme based on DQRCI. *Multimedia Tools and Applications* **79**, 6661–6687 (2020).
38. Grigoryan, A. M. & Agaian, S. S. Paired quantum Fourier transform with log 2 N Hadamard gates. *Quantum Information Processing* **18**, 1–26 (2019).
39. Grigoryan, A. M. & Agaian, S. S. New look on quantum representation of images: Fourier transform representation. *Quantum Information Processing* **19**(5), 148 (2020).
40. Cleve, R., & Watrous, J., Fast parallel circuits for the quantum Fourier transform, in *Proceedings 41st Annual Symposium on Foundations of Computer Science*, 526-536 (IEEE, 2000).
41. Kamiyama, M. & Taguchi, A. HSI color space with same gamut of RGB color space. *IEICE Transactions on Fundamentals of Electronics, Communications and Computer Sciences* **100**(1), 341–344 (2017).
42. Saravanan, G., Yamuna, G., & Nandhini, S. Real time implementation of RGB to HSV/HSI/HSL and its reverse color space models, in *2016 International Conference on Communication and Signal Processing (ICCSP)*, 0462-0466 (IEEE, 2016).

43. Yoshinari, K., Murahira, K., Hoshi, Y., & Taguchi, A., Color image enhancement in improved HSI color space, in 2013 International Symposium on Intelligent Signal Processing and Communication Systems, 429-434 (IEEE, 2013).
44. Yan, F., Li, N. & Hirota, K. QHSL: A quantum hue, saturation, and lightness color model. *Information Sciences* **577**, 196–213 (2021).
45. Chen, G.-L., Song, X.-H., Venegas-Andraca, S. E. & Abd El-Latif, A. A. QIRHSI: novel quantum image representation based on HSI color space model, Quantum Information Processing **21**(1), 5 (2022).
46. Li, M., Song, X. & El-Latif, A. A. A. EQIRHSI: enhanced quantum image representation using entanglement state encoding in the HSI color model. *Quantum Information Processing* **22**(9), 334 (2023).
47. https://sipi.usc.edu/database/database.php?volume=miscampimage=1#top
48. https://en.wikipedia.org/wiki/Test_Card_F
49. Estrada, E. Communicability cosine distance: similarity and symmetry in graphs/networks. *Computational and Applied Mathematics* **43**(1), 49 (2024).
50. Das, S. & Caruso, F. A hybrid-qudit representation of digital RGB images. *Scientific Reports* **13**(1), 13671 (2023).
51. Yao, X.-W. et al. Quantum image processing and its application to edge detection: theory and experiment. *Physical Review X* **7**(3), 031041 (2017).
52. Rong, W., Li, Z., Zhang, W. & Sun, L. An improved CANNY edge detection algorithm, in 2014 IEEE international conference on mechatronics and automation, 577-582. (IEEE, 2014)
53. https://scikit-image.org/docs/0.20.x/auto_examples/color_exposure/plot_rgb_to_gray.html#sphx-glr-auto-examples-color-exposure-plot-rgb-to-gray-py
54. https://en.wikipedia.org/wiki/Ashurbanipal

Acknowledgements

This research was sponsored by the Universiti Malaya Research Excellent Grant UMREG 068 - 2024 (UM.0000285/HRU.RC), and the Universiti Malaya Research Maintenance Fee RMFI2067-2021 (UM.0002145/HIP.IP).

Author contributions

Conceptualization, N. A., S. O., Y. K.,and N. G.; methodology, N. A. , Y. K., S. O. and N. G.; software, N. A.; validation, Y. K., S. O. and N. G.; formal analysis, Y. K. and N. F.; investigation, N. F., N.A., Y.K. and S. O.; writing original draft preparation, N. A., Y. K. and N. G.; writing review and editing, S. O., Y. K. and N. F.; visualization, N. G. and Y. K.; supervision, S. O.; project administration, S. O.; funding acquisition, S. O. All authors have read and agreed to the published version of the manuscript.

Declarations

Competing interests

The authors declare no competing interests.

Additional information

Correspondence and requests for materials should be addressed to S.J.O.

Reprints and permissions information is available at www.nature.com/reprints.

Publisher's note Springer Nature remains neutral with regard to jurisdictional claims in published maps and institutional affiliations.